Invited Articles

Toroidal cavitation by a snapping popper

Akihito Kiyama
Department of Biological and Environmental Engineering, Cornell University, Ithaca, New York 14853, USA and Department of Mechanical Science, Saitama University, 338-8570, Japan

Sharon Wang, Jisoo Yuk, and Sunghwan Jung
Department of Biological and Environmental Engineering, Cornell University, Ithaca, New York 14853, USA

(Received 30 March 2023; accepted 23 February 2024; published 19 March 2024)

Cavitation is a phenomenon in which bubbles form and collapse in liquids due to pressure or temperature changes. Even common tools like a rubber popper, which is a children's toy that rapidly changes its shape when snapped, can be used to create cavitation at home. As a rubber popper toy slams a solid wall underwater, toroidal cavitation forms. As part of this project, we aim to explain how an elastic shell causes cavitation and to describe the bubble morphology. High-speed imaging reveals that a fast fluid flow between a snapping popper and a solid glass reduces the fluid pressure to cavitate. Cavitation occurs on the popper surface in the form of sheet cavitation. Our study uses the axisymmetric Rayleigh-Plesset equation and the energy balance to capture the relationship between the bubble lifetime and the popper deformability. The initial distance between the popper and the wall is an important parameter for determining the cavitation dynamics. Presented results provide a deeper understanding of cavitation mechanics, which involves the interaction between fluid and elastic structure.

DOI: 10.1103/PhysRevFluids.9.030501

I. INTRODUCTION

Cavitation is a phase change process from liquid to gas (i.e., vaporization) due to an abrupt decrease in fluid pressure. Cavitation bubbles collapse onto solid objects and walls after nucleation, causing destructive erosion. For example, cavitation in a high-speed flow around a hydrofoil or a propeller damages their structure (e.g., [1–3]). It can significantly reduce the efficiency of marine propulsion and hydro turbine systems and cause design failures due to the excessive vibration. On the other hand, engineers use the impulsive fluid motion associated with cavitation bubbles in beneficial ways, e.g., for medical [4] and cleaning applications [5,6].

Researchers have been employing various experimental methods to create a spherical cavitation bubble [7]. For example, a short-pulsed laser was used to study bubble collapse and rebound behaviors [8–10]. The laser method allows researchers to study the high-precision behavior of cavitation bubbles down to nanosecond timescales. The electric spark method is used to create a single bubble at a low cost, as used in the study for bubble-particle interaction [11] and bubble dynamics in non-Newtonian fluid [12]. Ultrasonic transducers have also been used as an alternative to the electric spark method to create bubble cavitation [13,14].

Cavitation occurs not only in engineering systems but also in natural systems and everyday items. In nature, pistol shrimp use bubbles to stun their prey [15,16]. These bubbles are created by the shrimp's claw and can reach high temperatures and high pressure, killing small fish. Even in everyday activities, cavitation can be seen when one cracks the finger joint [17], drops water-filled vials [18]/tubes [19], or performs a party trick with a beer bottle [20]. Such events are caused by

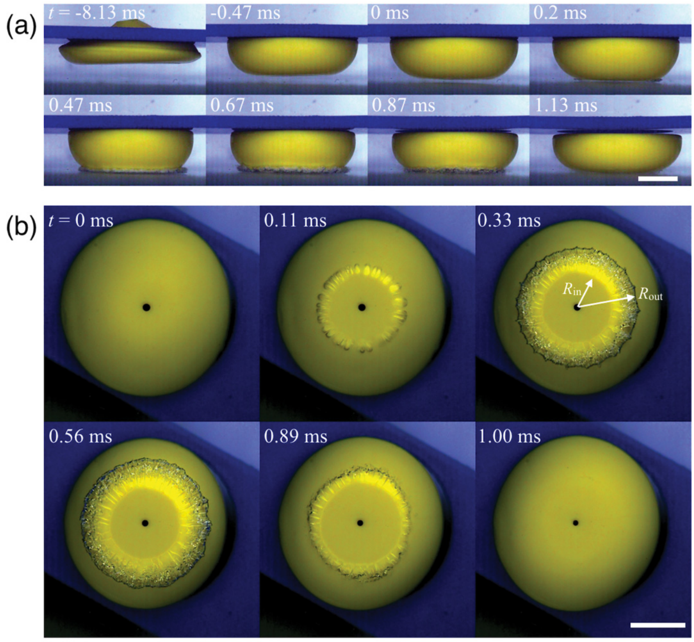

FIG. 1. (a) Side-view images of the underwater popper ($R_p \approx 16$ mm) approaching the glass substrate. The platform height was set at $H \approx 9$ mm (i.e., $H/R_p \approx 0.56$). (b) Bottom-view images of the same popper and cavitation dynamics. We used a 50% glycerol-water mixture (≈5 cSt) for visualization purposes. The platform height was set at $H \approx 12$ mm (i.e., $H/R_p \approx 0.75$). The scale bars represent 10 mm. Both images were edited to enhance the brightness/clarity. The images were originally presented at the Gallery of Fluid Motion competition (November 2022, Indianapolis, IN) and are reproduced from it [30]. We note that the black circle that appears on the center of the popper is a hole on the popper's top surface.

the formation of bubbles and their subsequent collapse, which releases energy in the form of shock waves with loud sound and heat.

Activating a rubber popper underwater can also create cavitation. The rubber popper is a famous children's toy, which is made of a rubbery material in the shape of a hemispherical shell. The unique feature of this inexpensive toy is its rapid shape change after being inverted. Upon activation, an inverted rubber popper quickly returns to its original hemispherical shape. The dynamic is called "snap-through" instability and is widely studied (e.g., [21,22]) and even used as an actuator for soft robotics [23,24]. Often times, the popper can jump up to a few meters in the air. Even underwater, the popper dynamics remains very fast. Figure 1 shows the formation of toroidal cavitation in an aqueous solution upon the slamming of the popper to the substrate. The bubble forms spontaneously within a thin gap between the popper and the substrate and lasts for $\sim O(1)$ ms. We note that the entire process seems similar to the cavitation reported upon the underwater collision between a solid object and substrate [25–27]. In these works, the cavitation onset was explained by either the depressurization upon rebound [28] or the high shear stress [29]. Both mechanisms may not be applicable to this particular toroidal cavitation resulting from a snapping popper (Fig. 1).

In this paper, we examine the cavitation phenomena caused by an elastic popper. First, we classify three types of cavitation and discuss their mechanism of cavitation onset. Systematic experiments suggest that a fast water flow squeezed out from a thin gap between the popper surface and the glass substrate dominates the toroidal cavitation, as implied by a conventional cavitation number [1]. We then focus on the morphology of the bubble (i.e., the lifetime and radius) and discuss it through the axisymmetric Rayleigh-Plesset equation. We also adopt the energy balance between the inverted popper and the fully expanded cavitation, and we discuss the physical meaning of the control parameter to provide a theoretical framework. The present paper provides insights into cavitation mechanics that are a result of fluid-elastic interaction.

II. METHODS

A. Preliminary experiments and observations

We performed a preliminary experiment to capture overall dynamics (see Appendix A, Fig. 8, for the details). A rubber popper has a hemispherical shape at rest. First, we inverted the rubber popper (i.e., inside-out) and mounted the inverted popper on a three-dimensional (3D)-printed platform. The platform was equipped with a hole, with an inner diameter of 3 cm. Since the popper was slightly lighter than water and could float, this platform was used to fix the popper's location. The inverted popper activates itself to snap after some time delay. With assistance from the platform, the popper moves towards the bottom of the container (i.e., the solid substrate) to interact with it. The whole activation process is illustrated in Appendix A (see Fig. 9). The timescale for the popper snap from the start to the end (i.e., the maximum stretch) lasts for $\sim O(10)$ ms (see Appendix B, Fig. 10). The initial height of the platform measured from the container bottom is the control parameter H. The standoff parameter H/R_p is defined as the initial popper location H normalized by the popper radius R_p, which is measured based on the base diameter of the popper D_p. The standoff parameter is varied for $0.5 \leqslant H/R_p \leqslant 1.4$. Five experiments were conducted for each condition.

We used commercially available poppers [31] of two different radii, $R_p \sim 16$ and ~ 22 mm. We assumed that Young's modulus will be $E \simeq 3.91$ MPa based on our curved-beam bending measurements for a small popper (see Appendix F, Fig. 19). The characteristic thickness of the popper, $h_p \approx 3$ mm, was measured at the rim of each cut popper, although it is worth noting that the thickness varies slightly along the arc. The poppers we used have a small hole on their top surface, as is visible in Fig. 1(b). We used deionized water as a working fluid, where the density and the vapor pressure were assumed to be $\rho \sim 1000\ \mathrm{kg/m^3}$ and $p_v \sim 2$ kPa. In Fig. 1, we used for visualization purposes a glycerol-water mixture ($\approx$50% by volume), whose viscosity is expected to be higher than the water ($\sim$5 cSt [32]). The change in viscosity does not have a significant influence on the overall dynamics. The Reynolds number $\mathrm{Re} = \rho V_r D_p/\mu$, where V_r (see the results and discussion) and D_p are the radial velocity of the flow and the diameter of the popper, respectively, remained much larger than unity. For instance, in the case of cavitation onset, the speed of flow can reach $V_r \sim 14$ m/s (by assuming $\mathrm{Ca} \sim 1$). We then obtain $\mathrm{Re} \sim 4.48\times10^5$ for water. For a glycerol-water mixture, the Re value might reduce to $\mathrm{Re} \sim 8.96\times10^4$, which is, however, still larger than unity. The use of the glycerol-water mixture slightly smoothes the bubble surface and, more importantly, assists in visualizing the cavitation formation process, as discussed later. The experiments were performed in Ithaca, NY. We assumed the atmospheric pressure to be $p_0 \sim 101$ kPa.

The dynamics of the popper were captured by synchronized high-speed cameras. The bottom-view images were recorded by two Photron Fastcam NOVA (5000 frames per second) either directly or through mirrors. The cavitation onset was manually detected, and bubble lifetime t_{life} and bubble size R_{in} and R_{out} were estimated. The side-view images were filmed by Photron Fastcam SA-Z (5000 frames per second). To estimate the bubble lifetime t_{life}, we defined $t = 0$ as one frame prior to the confirmed onset of the bubble. The first-order approximation of the uncertainty would be $t_f/2 \approx 0.1$ ms, where t_f is the interval between two consecutive high-speed images (i.e., 1/frame rate).

We first show the general trend of the size of the cavitation bubble R_{in} and R_{out} as a function of the platform position H [Fig. 2(a)]. Blue and red markers show the data from the preliminary experiment, while the black ones represent the main experiment result as explained in the following section. By definition [see Fig. 1(b)], the outer radius R_{out} (filled markers) is always bigger than the inner one R_{in} (open markers). But their trend as a function of H remains similar to each other for both popper sizes ($R_p = 16$ and 22 mm). It is noted that a larger popper can create a larger bubble while maintaining a similar downward trend against H. The bubble lifetime t_{life} also goes with a similar trend against H [Fig. 2(b)].

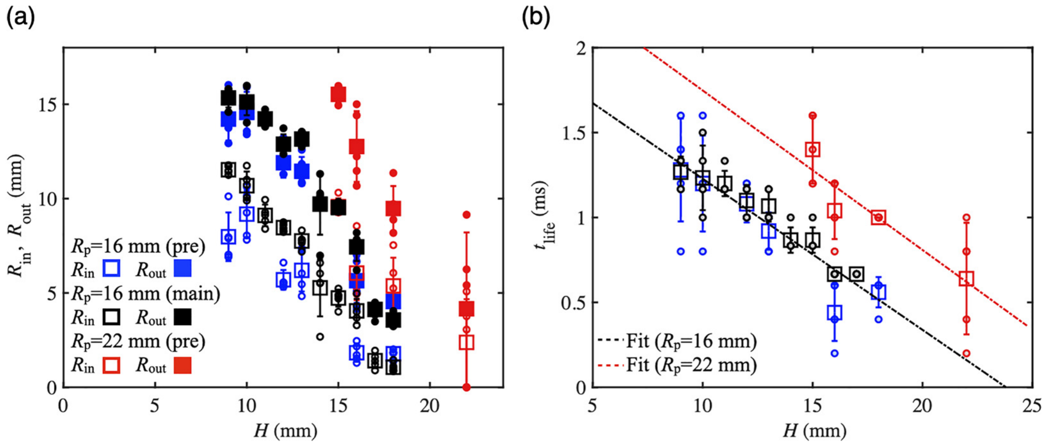

FIG. 2. (a) Radius of the cavitation R_{in} (open markers) and R_{out} (filled markers) as a function of the platform position H. Colors distinguish the popper sizes (blue for $R_p = 16$ mm in the preliminary experiment, black for $R_p = 16$ mm in the main experiment, and red for $R_p = 22$ mm in the preliminary experiment). We note that we have five trials at each condition (marked by dots) to obtain the mean value (square) and standard deviation (error bar). (b) Lifetime of the cavitation t_{life} as a function of the platform position H. Trend lines are $t_{life} = -0.089H + 2.118$ (R-squared value: 0.7306) for a smaller popper (a black dashed line, preliminary and main experiments combined) and $t_{life} = -0.094H + 2.687$ (R-squared value: 0.5891) for a larger popper (a red dashed line).

The preliminary experiment revealed that the toroidal cavitation we presented in Fig. 1 can be observed in only limited experimental conditions. If a popper is released too close to the substrate (i.e., small H), the popper cannot be accelerated fast enough to cavitate fluid before interacting with the substrate. We did not observe the cavitation, or we observed only a partial toroidal bubble at $H = 7$ mm for $R_p \sim 16$ mm (not shown in Fig. 2 and not included to compute trend lines). Also, the cavitation bubbles except for the ring-type bubble (discussed in the following section) vanish if H is very large. The dimensionless popper location H/R_p seemed to be the primary parameter to differentiate the phenomena. We note that our focus is on the fluid mechanics of cavitation, and therefore we choose H/R_p as the control parameter.

B. Main experiments

After performing the preliminary experiment, it became evident that closeup observations were necessary. We performed the three-dimensional imaging by employing a simpler setup and higher magnification [Fig. 3(a)] to estimate the inner shape and slamming speed of the popper right before the cavitation onset. The frame rate of the two Photron NOVA high-speed cameras was set at 6000 frames per second. The spatial resolutions were almost identical to each other (25.56 and 27.45 pixels/mm). The image size was 1024×1024 pixels. In this experiment, we selected one popper, whose radius was $R_p \sim 16$ mm and whose surface was painted by black dots (see Fig. 4), as a representation. Image pairs were cross-correlated through a DLTdv8 digitizing tool [33] to estimate the deflection of the inverted popper surface. The software is available for free and can be run as the MATLAB application. Dotted patterns were tracked semi-manually to compute values in not only the x and y but also the z coordinates. This method has certain limitations, including potential inaccuracies due to the finite size of the surface dots. We analyzed only a limited number of dots along the same angular direction each time so that we might minimize the impact of the uneven shape of the popper on our observations (see Appendix C). Additionally, since the number of surface dots was limited, we relied on a fourth-order polynomial fitting to approximate the outline of the popper surface. The vertical speed of the slamming popper, U_{popper}, can be estimated as

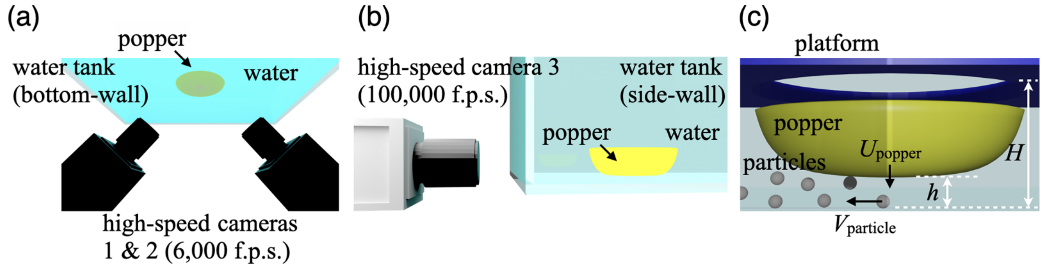

FIG. 3. (a) Schematic of the bottom-view measurement by employing two high-speed cameras (not to scale). (b) Schematic of the side-view measurements with and without tracer particles [see also the left- and right-hand side portions of (c), not to scale]. Some of the measured quantities (H, h, U_{popper}, and V_{particle}) are presented in (c), while they were calculated in separate measurements.

$U_{\text{popper}} = \Delta z_{\text{popper}}/\Delta t_1$, where Δz_{popper} is the vertical displacement of the popper center for a short period of time Δt_1 before cavitation onset ($\Delta t_1 = 1$ ms). We tested 10 different H levels (from 9 to 18 mm, $0.56 \leqslant H/R_p \leqslant 1.13$) and repeated the measurement five times. We also used these captured images to measure the inner and outer bubble radii R_{in} and R_{out}, as well as the bubble's

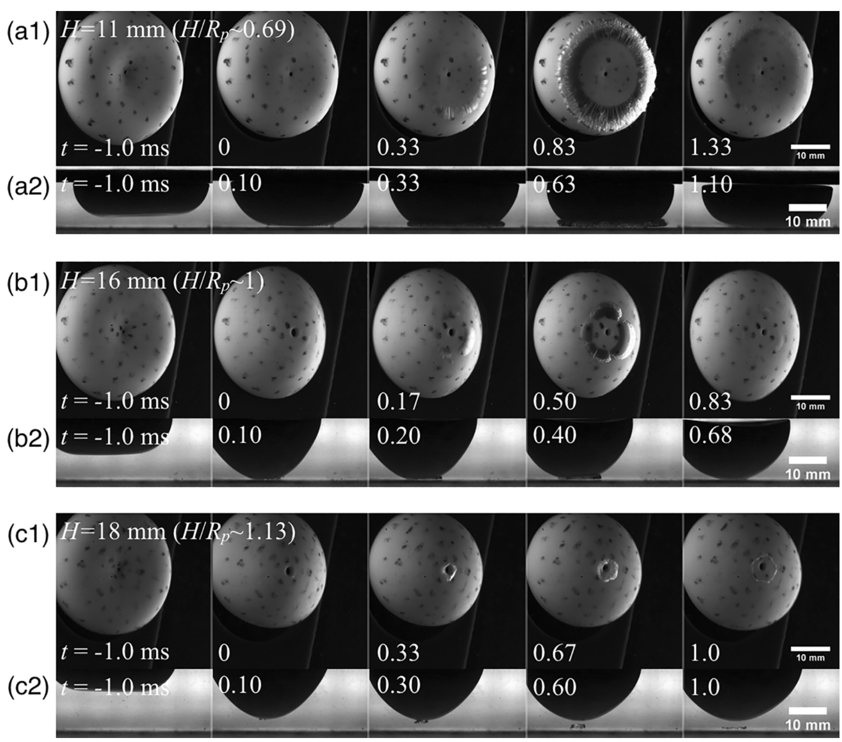

FIG. 4. High-speed images of cavitation phenomena upon popper slamming (R_p ~16 mm). (a1) Angled bottom-view of the toroidal bubble at $H/R_p \sim 0.69$. The dark dots and tilt are used to measure 3D shapes. The frame rate was 6000 frames per second. (a2) Side-view images of the toroidal bubble separately filmed at the same condition with a frame rate of 100 000 frames per second. (b1),(b2) High-speed images of the bubble in the transition regime ($H/R_p \sim 1$). (c1),(b2) High-speed images of the vortex-ring type bubble formed at the tip of the popper ($H/R_p \sim 1.13$).

lifespan t_{life} (see Appendix C, Fig. 12 for more details). We note that $t = 0$ was defined as one frame prior to the confirmed onset of the bubble.

We also performed two side-view measurements [see Fig. 3(b)]. One of them was to measure the flow speed right before the cavitation onset. Silver-coated ceramic particles with a typical diameter of $d \sim 85$ μm were seeded [see the left-hand side of Fig. 3(c)]. The Stokes number St for the particles was estimated to be $\mathrm{St} \sim 0.13 < 1$, suggesting a reasonable traceability (see Appendix D for the estimation). A Photron SA-Z high-speed camera could achieve a spatial resolution of ~32 pixels/mm (image size: 640×280 pixels) while maintaining a high temporal resolution (100 000 frames per second). We kept using the same popper (R_p ~16 mm) while changing the release height H for five different levels (from 9 to 18 mm, $0.56 \leqslant H/R_p \leqslant 1.13$). Particle tracking was performed via the free software TRACKER (e.g., [34]) for 0.3 ms until cavitation started. Unlike conventional particle tracking methods that employ a laser sheet, we utilized continuous LED lighting. This is because the popper surface can obstruct the laser sheet in a thin fluid gap. As a measure of the flow speed, the radial speed of the particle, $V_{\text{particle}} = \Delta r_{\text{particle}}/\Delta t_2$, was estimated, where Δr is the radial displacement of the particle for a short period of time Δt_2 before cavitation onset ($\Delta t_2 = 0.1$ ms). We note that we assumed the popper and fluid dynamics were to be axis-symmetric. While the particle dispersion and popper dynamics are not exactly the same for each trial, the general behavior was confirmed to be similar enough based on five trials (see Appendix D, Fig. 16). We also note that the fluid gap between the popper and substrate was extremely thin (less than 1 mm). This resulted in difficulties in attaining a high density of particles, especially near the popper's center. Furthermore, the tracer particles' movement near the substrate may be influenced by the viscous boundary layer. Therefore, the results from this measurement likely estimate the lower limit of the fluid velocity expelled from the fluid gap.

We also filmed the side-view images of the same popper (R_p ~16 mm) slamming the container bottom in water without particles to obtain a better understanding of the thickness of the fluid gap between the popper and substrate, h, and that of the bubble [see also the right-hand side of Fig. 3(c)]. We used a Photron SA-Z high-speed camera at 100 000 frames per second at 15.6 pixels/mm (image size: 640×280 pixels). The illumination was provided by the continuous LED lights. The gap h is measured at one frame earlier than the cavitation onset. Experiments were repeated five times for each condition (from 9 to 18 mm, $0.56 \leqslant H/R_p \leqslant 1.13$).

The conditions for the experiments performed are summarized in Table I. In addition to the above-mentioned experiments, we also measured the forces involved during the snapping of the popper and the Young's modulus of the popper material. The details of these supporting experiments can be found in Appendixes E and F (see Figs. 17 and 18 for the force, and Fig. 19 for the Young's modulus). It should be noted that our analysis primarily focuses on the initial onset of the bubble, though we also observed instances of secondary cavitation (see Appendix B and Fig. 10, and Appendix G and Fig. 20). We also performed supplementary experiments by employing a popper without a hole at the apex. The details can be found in Appendix G.

III. RESULTS

A. Detailed observations

We observed three different bubble dynamics: the toroidal cavitation, the vortex-ring-type bubble, and the transition. The first to be discussed is the toroidal cavitation that was mentioned in the preliminary observation (Fig. 1). As shown in Fig. 4(a1), bubbles form from the middle of the popper surface and then expand, maintaining a toroidal shape if $H/R_p \ll 1$. The bubbles are formed as a sheet-like cavitation occurs on the popper surface [see also Fig. 1(b)]. The bubble formation seems to be similar to the cavity formation upon a sphere water entry [35], where the gas phase expands from the three-phase contact point. From the side, it can be clearly seen that when the bubble begins to form, there is a thin gap between the bottom of the popper and the substrate [see $t = 0.1$ ms in Fig. 4(a2), and $t = 0.2$ ms in Fig. 1(a)]. We note that the bubble does not form as the symmetric

TABLE I. Summary of experimental conditions. In the preliminary experiment, we employed two different poppers to identify the primary parameter (i.e., H/R_p). The main experiment focused on investigating its influence with finer resolutions. We also performed supporting experiments, the details of which can be found in Appendixes E–G. We note that in our supplementary experiments without a hole, we repeated each experiment at least five times depending on the condition (marked with $*1$). The measurements were performed with a high-speed camera positioned for bottom-view recordings at a reduced frame rate [Photron SA5, 10 000 f.p.s. (marked with $*2$)].

R_p (mm)	H (mm)	H/R_p	Number of conditions × trials	Experiment type
16	7–18	0.438–1.13	7×5	Preliminary
22	12–22	0.545–1.00	5×5	
16	9–18	0.563–1.13	10×5	Main (bottom view)
16	9–18	0.563–1.13	5×5	Main (particle tracking)
16	9–18	0.563–1.13	10×5	Main (side view)
16	9–21	0.563–1.31	6×5	Supplementary (force)
22	13–22	0.591–1.00	5×5	
16	N/A	N/A	1×5	Supplementary (Young's modulus)
16	9–18	0.563–1.13	$10\times5^{*1}$	Supplementary (without a hole, bottom view^{*2})

torus when H/R_p is too small, as noted in the preliminary experiment at $H/R_p \sim 0.44$. From the bottom view in the main experiment, we observed this partial cavitation when $H/R_p \sim 0.56$ as well as in some of the $H/R_p \sim 0.63$ trials. The fully developed toroidal bubble was observed within the range starting from $H/R_p \sim 0.63$ up to $H/R_p \sim 0.81$.

We observed another unique bubble at the other end of the parameter space (i.e., $H/R_p \gg 1$). The bubble formed not from the midsurface but at the tip of the hole on the popper [see $t = 0.33$ ms in Fig. 4(c1)]. The side-view images indicate that the vortex ring-type bubble is ejected from the hole at some speeds and levitates in the gap for a while [Fig. 4(c2)]. The mechanism of bubble onset is different from the toroidal cavitation at a smaller H/R_p. It appears to occur independently of the interaction between the popper and the substrate. A key factor seems to be the velocity difference between the core and outer regions of the bubble. Notably, we did not observe the formation of vortex-ring-type bubbles with a popper without a hole at the apex, underscoring the importance of this structural feature (for a detailed discussion, see Appendix G). We note that the popper can oscillate several times after the initial snap, leading to a series of interactions associated with a form of the secondary toroidal cavitation (see also Appendix B and Fig. 10).

The third regime is the intermediate one. The bubble shows a somewhat ringlike shape [Fig. 4(b1)] but is not as uniform as the toroidal cavitation. The breaking of the symmetry starts to appear as "cracks" on the bubble surface from $H/R_p \sim 0.88$ and becomes apparent when $H/R_p \sim 1.0$ [refer to $t = 0.50$ ms in Fig. 4(b1)]. The gap h between the popper and the substrate becomes very thin and nearly invisible [$t = 0.1$ ms in Fig. 4(b2)]. The popper perhaps recovers its original stable shape as H/R_p approaches 1.0, but still generates cavitation near the center of the popper due to the interaction with the substrate.

The three-dimensional imaging enabled us to visualize the complex inner shape of the popper while it is snapping. Figure 5 shows the estimated shape of the popper at different moments (from $t = -3$ to 1 ms). The reference time $t = 0$ ms represents one frame earlier than the cavitation onset. When $H/R_p \ll 1$ [Fig. 5(a)], the popper maintains either a flattened or even inverted bottom shape at the time of cavitation. The location of the extreme $R_{\rm rim}$ at $t = 0$ ms, where the distance between the popper and the substrate becomes minimum, was computed and marked by a star in Fig. 5(a). A similar popper bottom shape was observed for $0.56 \leqslant H/R_p \leqslant 0.81$. As H/R_p increases, the popper recovers the hemispherical shape when it approaches the substrate ($t \sim 0$ ms). A stretched popper for $H/R_p \sim 1.0$ touched (or approached close enough) the substrate as suggested by the

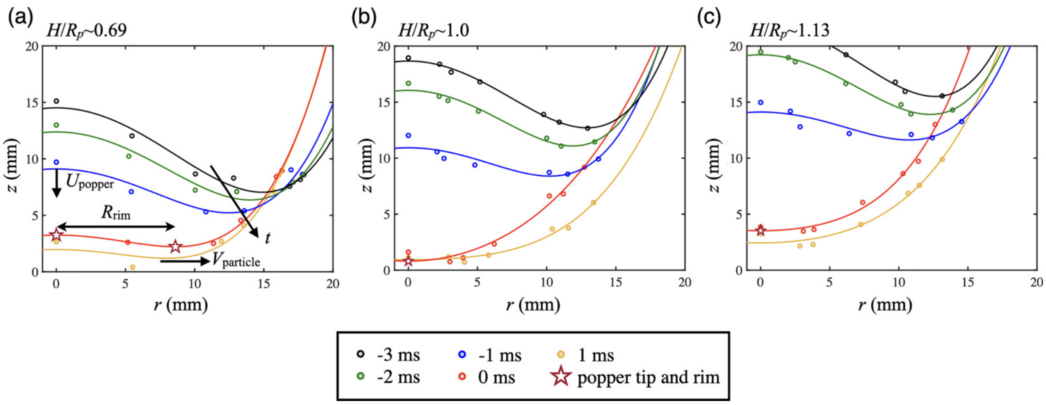

FIG. 5. The bottom shape of the popper ($R_p \sim 16$ mm) is estimated by the three-dimensional imaging at a frame rate of 6000 frames per second. $r = 0$ represents the location of the popper center. Colors distinguish the times from $t = -3$ to 1 ms. The reference time $t = 0$ ms represents the one frame earlier than the cavitation onset. Solid lines are computed based on the popper height at each distance r (marked by dots) from the center by adopting the fourth-order polynomials while assuming that the popper shape is axis-symmetric. Stars represent the popper center and $R_{\rm rim}$ at $t = 0$ ms when available. The height of the substrate $z = 0$ is set arbitrarily but remains the same for all three panels. All three panels share the legend shown in a box underneath. The experimental conditions were $H/R_p \sim 0.69$ for (a), $H/R_p \sim 1.0$ for (b), and $H/R_p \sim 1.13$ for (c). We note that the arrows in (a) indicate the direction of the speeds of popper center $U_{\rm popper}$ and seeded particles $V_{\rm particle}$ that we present in Fig. 6(a) [see also Fig. 3(c)].

slight movement of the popper tip between $t = 0$ and 1 ms [Fig. 5(b)]. When $H/R_p \gg 1$, the popper is still moving when it induces the vortex-ring type bubble [Fig. 5(c), $t = 0$ and 1 ms]. The popper oscillates and travels toward the substrate [see also Fig. 4(c2)]. Comparing the traveling distance of the popper center between $t = -1$ ms (blue line) and $t = 0$ ms (red line) in Figs. 5(a)–5(c), it is visible that the speed of the popper increased as H/R_p increased.

B. Cavitation mechanism

Regardless of the bubble dynamics type, the liquid pressure needs to be reduced significantly to cavitate. The cavitation number Ca is a powerful tool to scale the likelihood of cavitation (e.g., [1]), which compares the pressure threshold $p_0 - p_v$ and pressure drop Δp as

$$\mathrm{Ca} = \frac{p_0 - p_v}{\Delta p}. \tag{1}$$

Here, p_0 and p_v are, respectively, the atmospheric ($p_0 = 101$ kPa) and liquid vapor ($p_v = 2$ kPa for water) pressures. This dimensionless number tells us that the lower the cavitation number, the higher the chance of cavitation. An appropriate representation of Δp may vary depending on the mechanism of cavitation [20]. In this manuscript, we adopted the conventional dynamic pressure representation to estimate it as $\Delta p \sim \frac{1}{2}\rho V^2$ [i.e., $\mathrm{Ca} \sim (p_0 - p_v)/\frac{1}{2}\rho V^2$], where V is the characteristic flow speed of this expansion flow [36].

The popper center might move fast enough to cavitate water when H/R_p is large enough. Circles in Fig. 6(a) show the speed of the popper center, $U_{\rm popper}$, which is estimated by the three-dimensional imaging data (see also Fig. 5). In general, $U_{\rm popper}$ increases as H/R_p increases. It showed a somewhat flat response for larger H/R_p values, perhaps because the popper achieved the maximum stretch. The popper speed $U_{\rm popper}$ reached $U_{\rm popper} \sim 11$ m/s, which gave us a cavitation number of $\mathrm{Ca} \sim 1.64$, where $V \sim U_{\rm popper}$. Because this $U_{\rm popper}$ is the averaged speed over the relatively long time interval ($\Delta t_1 \sim 1$ ms), we can safely assume that the instantaneous speed is faster, and might satisfy $\mathrm{Ca} < 1$.

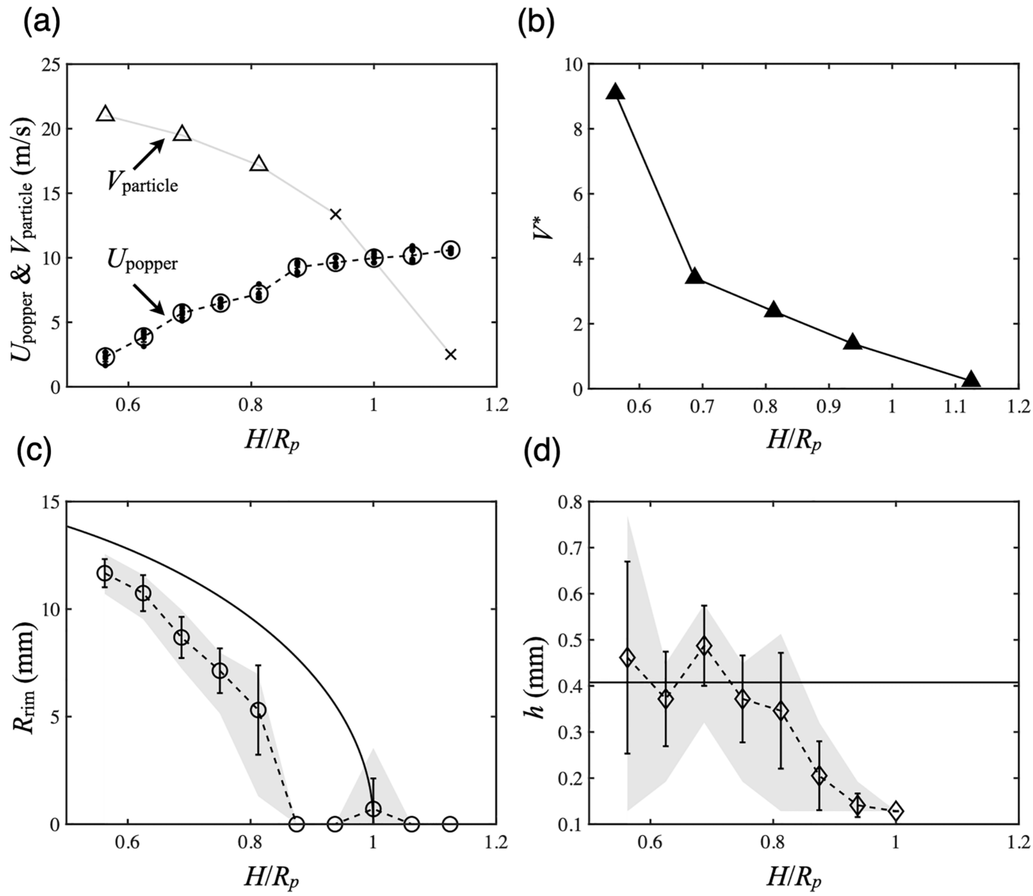

FIG. 6. (a) Circles show the vertical velocity of the popper, U_{popper}, measured through the three-dimensional imaging tracking method as shown in Fig. 5. Open circles represent the mean value of five trials under the same condition, while small dots denote individual trials. Triangles show the speed of particles in the radial direction, V_{particle}, measured through particle tracking below the popper's bottom surface. The fastest particles for larger H/R_p are found outside the popper's bottom surface ($r > R_{\text{rim}}$), marked by crosses. (b) The ratio of speeds $V^* = V_{\text{particle}}/U_{\text{popper}}$ calculated from the values in Fig. 6(a) is plotted as a function of H/R_p. (c) Circles show the location of the popper's surface closed to the substrate (e.g., Fig. 5), R_{rim}. Markers and error bars are the mean and standard deviation calculated from five trials, respectively. A gray shaded region outlines the maximum and minimum values for each condition. A solid line shows the first-order approximation $R_{\text{rim}} \sim R_p\sqrt{1-(H/R_p)^2}$. The discrepancy from the data may suggest that the popper stretches beyond its original length due to elasticity. (d) The thickness of the gap h was measured through side-view imaging (marked by the diamonds). Markers and error bars are the mean and standard deviation calculated from five trials, respectively. A gray shaded region outlines the maximum and minimum values for each condition. A solid line denotes $h \sim 0.4$ mm, which was calculated from the data for $0.56 \leqslant H/R_p \leqslant 0.81$. It is noted that we did not measure h when $H/R_p > 1$, as the vortex-ring-type bubbles formed regardless of the distance from the substrate.

It suggests that the vortex-ring-type bubble for $H/R_p \gg 1.0$ [the third regime, Fig. 4(c)] occurs solely due to the fast snapping of the tip of the popper center and thus does not require the assistance from the substrate.

The toroidal cavitation was observed when $H/R_p \leqslant 0.81$, as discussed earlier, where U_{popper} (i.e., the measure of the highest speed that the popper can achieve before the cavitation onset) was even not fast enough to cavitate water. In such cases, the flow near the substrate could, however, be fast enough. The result of the particle tracking from the side view shows that the particles below the flattened popper bottom [marked by the triangles in Fig. 6(a)] can achieve Ca < 1 (i.e., $V > 14.1$ m/s). We propose that toroidal cavitation occurs due to a rapid squeezing flow, which is greater than the speed of the popper snapping (i.e., $V \sim V_{\text{particle}} > U_{\text{popper}}$) when a thin gap is formed. It is noted that the speed of the fastest particle, V_{particle}, decelerates as H/R_p increases. The transition of these two velocity scales is shown in Fig. 6(b). It shows the ratio of speeds $V^* = V_{\text{particle}}/U_{\text{popper}}$ as a function of H/R_p. It indicates an enhanced radial flow relative to the vertical popper motion at a smaller H/R_p, which aligns intuitively with the aforementioned discussion.

To scale the order of magnitude of the speed of the squeezed flow, we consider a simple mass conservation. We denote the speed of the radial flow in the thin gap as V_r. Here, we are interested in the fluid dynamics within a very short time period, right before the onset of cavitation, and to scale the velocity increment of the squeezed liquid. The vertical compression (flow rate: $Q_{\text{in}} \sim \pi R_{\text{rim}}^2 U_{\text{popper}}$) is induced by the slamming popper, while the squeezed flow is expelled through the outlet (flow rate: $Q_{\text{out}} \sim 2\pi R_{\text{rim}} h V_r$). In terms of the rim location, Fig. 6(c) shows the location of the extreme R_{rim} as a function of H/R_p. By neglecting any water leakage through a hole on the popper's center as well as changes in h and R_{rim} over a brief time span, and assuming incompressibility, we may approximate $Q_{\text{out}} \simeq Q_{\text{in}}$ as

$$2\pi R_{\text{rim}} h V_r \simeq \pi R_{\text{rim}}^2 U_{\text{popper}}. \tag{2}$$

The radial velocity of fluid that we want to scale here is thus

$$V_r \sim \left(\frac{R_{\text{rim}}}{2h}\right) U_{\text{popper}}. \tag{3}$$

It is obvious that the above expression represents a somewhat simplified approach. This simple scaling law still captures the extremely fast flow speed expected from that of particles [Fig. 6(a)]. While the fine scale of the gap h makes it challenging to discuss its trend, our data show the gap could be $h \sim 0.4$ mm for $H/R_p \leqslant 0.81$ [a gray line in Fig. 6(d)]. This implies that a flow speed can be as fast as $V_r \sim [R_{\text{rim}}/(2h)]U_{\text{popper}} \sim 30 - 50$ m/s, which is supposed to be fast enough to cavitate water. We note that the particle speed V_{particle} is the measure of the lower bound of the flow speed as discussed in Appendix D. The above observations agree with our hypothesis that the fast flow squeezed out from the thin gap between the popper and substrate drives the toroidal cavitation.

We note that the cavitation in the transition region might occur slightly differently than the toroidal cavitation. R_{rim} could not be computed [Fig. 6(c)] and thus the popper perhaps reached (or approached close enough to) the substrate. The scaling for the water flow in the gap no longer holds. It was in the same line with our side-view visualization that showed the gap h for $H/R_p \sim 1$ was not visible or was negligibly small [Fig. 6(d)]. In the particle tracking, the fastest particles were found outside of the popper bottom surface [i.e., $r > R_{\text{rim}}$, marked by the crosses in Fig. 6(a); see also Fig. 16 in Appendix D].

It is also important to compare this unique phenomenon to those reported in similar settings. In the previous study, the cavitation bubbles, which were formed immediately after the collision of the rigid sphere, were spherically nucleated around the impact point [28]. In contrast, the bubbles in our study nucleate annually without physical contact between the popper and the substrate. We do not observe bubbles in the central region, indicating that pressure reduction is localized in the annulus region, which is perhaps assisted by the snap-through dynamics of the popper. The bubbles in the annulus then merge to form a toroidal bubble during the evolving stage [Fig. 1(b), $t = 0.33 - 0.89$ ms]. We also note that our experiment does not provide sufficient evidence to determine the contribution of stress-induced cavitation [29]. The shear stress might scale as $\sigma \sim \mu(\partial V_r/\partial z) \sim \mu(V_r/h)$ by assuming a Couette flow. This simple scaling predicts $\mu(V_r/h) \sim 50$ Pa $\ll (p_0 - p_v)$ for the toroidal cavitation cases, where $\mu \sim 1$ mPa s, $V_r \sim 20$ m/s, and $h \sim$0.4 mm are assumed. However, it might become dominant in the transition regime (the second regime, $H/R_p \sim 1$) as the gap h can be extremely thin [Fig. 6(d)]. Regarding the mechanism for the transition regime, we will discuss it further in terms of the popper dynamics in the next section.

C. Cavitation morphology

In addition to the scaling on the liquid squeezed velocity, we will discuss the bubble morphology and its relation with the popper dynamics. We first discuss how the lifetime of the cavitation bubble is related to its size through the equation of motion (i.e., the Rayleigh-Plesset equation [37,38]). For simplicity, we make a crude assumption that bubble dynamics are two-dimensional and purely radial. We also neglect the movement of the inner radius ($R_{\rm in}$) within the lifetime of the bubble. These assumptions imply that we derive a scaling law for cavitation bubbles in the toroidal cavitation and the transition regimes, where the bubble dynamics are largely restricted to the two-dimensional. We note that the vortex-ring-type bubble requires the translational speed taken into account [39], which is not the scope of this study. We may use the axisymmetric Rayleigh equation (e.g., [40]) in terms of the bubble radius R, as

$$\left[\left(\frac{dR}{dt}\right)^2 + R\frac{d^2R}{dt^2}\right]\log\left(\frac{R}{R_\infty}\right) + \frac{1}{2}\left(\frac{dR}{dt}\right)^2 = \frac{p_0 - p_v}{\rho}. \tag{4}$$

We neglected the influence of viscosity, surface tension, and dissolved gas. With the approximation of $\log(R_\infty/R) \approx 1$ [41], the left-hand side of the above equation becomes $R\,(d^2R/dt^2) + 1/2(dR/dt)^2 \approx (d^2R^2/dt^2)/2$. One might notice that a prefactor for the second term on the left is slightly different from $3/2$ [41], which, however, does not significantly alter the final results. Finally, it became

$$\frac{d^2R^2}{dt^2} \approx 2\left(\frac{p_v - p_0}{\rho}\right). \tag{5}$$

We solve this equation in terms of the bubble collapse stage to estimate the characteristic timescale τ. We use the initial conditions $R = R_{\rm out}$ and $dR/dt = 0$ at $t = 0$, and then obtain

$$R^2 = R_{\rm out}^2 + \left(\frac{p_v - p_0}{\rho}\right)t^2. \tag{6}$$

The timescale τ, which a bubble requires to shrink from $R = R_{\rm out}$ at $t = 0$ to $R = R_{\rm in}$ at $t = \tau$, can be scaled as

$$\tau \sim \sqrt{\left(R_{\rm out}^2 - R_{\rm in}^2\right)\frac{\rho}{p_0 - p_v}}. \tag{7}$$

Equation (7) describes the experimental data well [Fig. 7(a)], despite the simplifications we made. Both sides are normalized by the Rayleigh-type factor $R_p\sqrt{\rho/(p_0 - p_v)}$. Different colors represent different popper sizes R_p. Red and blue markers show data from the preliminary experiment, while black markers represent the ones from the main experiment. Squares represent the mean values over the five trials with the error bars indicating the standard deviation. Individual trials were marked by dots. We note that we present bubble data in only the fully toroidal and transition regimes. It is visible that data series collapsed well and showed an incremental trend. The best fit (i.e., solid line) $t_{\rm life}/[R_p\sqrt{\rho/(p_0 - p_v)}] = 1.075\,[(R_{\rm out}^2 - R_{\rm in}^2)/R_p^2]^{\frac{1}{2}}$ captures the general behavior for both popper sizes, while the prefactor differs from 2. The ambient pressure may influence the bubble dynamics, although our experiments were conducted under atmospheric pressure. We note that a few data points are showing nonzero $t_{\rm life}$ values while $(R_{\rm out}^2 - R_{\rm in}^2)/R_p^2 = 0$ in Fig. 7. In these cases, the bubbles formed partially but not fully developed annual shapes at small H/R_p and thus the radii were not identified. We note that the bubble at $H/R_p \sim 1.13$ was clearly the vortex-ring type one [Fig. 4(c)] and thus excluded from the plot.

To connect the bubble and the popper dynamics, we consider the energy balance between them. For simplicity, we assume that an elastic potential energy, $Y_{\rm elastic}$, which is stored in the indented hemispherical shell, is released into the water bath where the dissipation is negligible. The released energy will be fully converted into the cavitation process to form an annulus-shaped bubble without

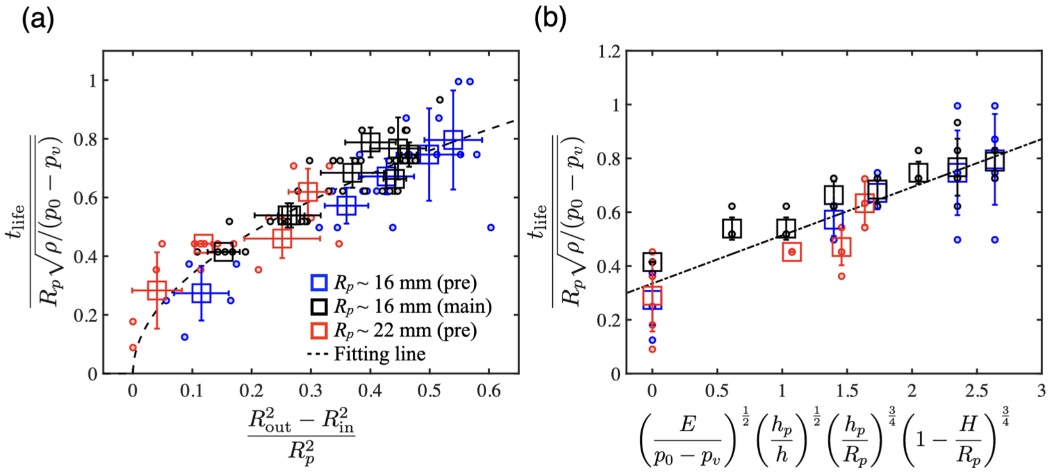

FIG. 7. Comparison between the normalized bubble lifetime $t_{\text{life}}/[R_p\sqrt{\rho/(p_0-p_v)}]$ vs the bubble size $(R_{\text{out}}^2 - R_{\text{in}}^2)/R_p^2$. The same data set was used as that in Fig. 2. Squares represent the mean value over five trials that are marked by dots. The error bars are showing the standard deviation. Colors distinguish the typical popper size at rest. The fitting line shows a trend, where the equation was estimated to be $t_{\text{life}}/[R_p\sqrt{\rho/(p_0-p_v)}] = 1.075\ [(R_{\text{out}}^2 - R_{\text{in}}^2)/R_p^2]^{\frac{1}{2}}$ (R-squared value: 0.702). (b) Comparison between the normalized bubble lifetime and the timescale based on the elastic potential energy, which was found in Eq. (10). The same representation of the data as that in (a) holds. The fitting line is found to be $t_{\text{life}}/[R_p\sqrt{\rho/(p_0-p_v)}] = 0.179[E/(p_0-p_v)]^{\frac{1}{2}}(h_p/h)^{\frac{1}{2}}(h_p/R_p)^{\frac{3}{4}}(1-H/R_p)^{\frac{3}{4}} + 0.335$ (R-squared value: 0.686).

any losses and thus be balanced with the work required to open up the bubble at its maximum size. A simple energy balance can yield

$$\left(R_{\text{out}}^2 - R_{\text{in}}^2\right) \sim \left(\frac{Y_{\text{elastic}}}{\pi\ h(p_0-p_v)}\right), \tag{8}$$

where h is the characteristic lengthscale of an annulus-shaped bubble (i.e., the toroidal bubble hereafter for simplicity), which is assumed to be the gap thickness between the popper and the substrate [$\simeq$0.4 mm from Fig. 6(d)]. The elastic potential energy Y_{elastic} can be approximated through the indentation force F [42] as

$$Y_{\text{elastic}} \sim \int F\ de \sim \frac{2}{3}\frac{E\ h_p^{\frac{5}{2}}}{R_p}e^{\frac{3}{2}} \sim \frac{2}{3}\frac{E\ h_p^{\frac{5}{2}}}{R_p}(R_p - H)^{\frac{3}{2}}. \tag{9}$$

Parameters E, h_p, and e are Young's modulus, the characteristic thickness of the popper, and the depth of indentation, respectively. The indentation depth e, relative to its equilibrium state, is scaled as $e \sim (R_p - H)$ based on the first-order geometrical consideration (neglecting the stretch of the popper) with the initial height of the platform, H. We note that the main objective here is to understand the mechanisms of the cavitation process, primarily induced by the instantaneous motion of the lower side of the popper. Hence, our model reflects the energy differences between two critical moments: right before and after the cavitation bubbles occur, instead of focusing on the initial and final states of the poppers deformation. It means that we neglected the influence of the surrounding flow before cavitation on the cavitation dynamics. We also note that we assumed the Young's modulus E and the popper thickness h_p to be constants for simplicity. Hereafter, we use the Young's modulus of $E = 3.91$ MPa from our curved-beam bending tests (see Appendix F, Fig. 19) and the popper thickness of $h_p \approx$3 mm measured at the rim of the cut popper, although h_p varies slightly along its arc.

We note that the scaling above is valid for a thin shell [42], meaning that the shell thickness is significantly smaller than its radius, thus satisfying the condition $h_p/R_p \ll 1$ [43]. Although the exact threshold for this condition remains unclear to the best of our knowledge, previous research suggests that deviations from the thin shell theory start in the range of $0.152 \leqslant h_p/R_p \leqslant 0.222$. Our smaller popper has a ratio of $h_p/R_p \sim 0.188$, which is in a transition regime. Still, we assume that the thin shell approximation is valid for our experimental conditions.

In Eq. (9), it is visible that the parameter H/R_p governs the elastic potential energy Y_{elastic}. Plugging Eqs. (8) and (9) into Eq. (7) finally gives us the relationship as

$$t_{\text{life}} \sim \sqrt{\frac{Y_{\text{elastic}}}{\pi h(p_0 - p_v)} \frac{\rho}{p_0 - p_v}} \rightarrow \frac{t_{\text{life}}}{R_p\sqrt{\rho/(p_0 - p_v)}} \sim \sqrt{\frac{E}{p_0 - p_v} \frac{h_p}{h} \left(\frac{h_p}{R_p}\right)^{\frac{3}{2}} \left(1 - \frac{H}{R_p}\right)^{\frac{3}{2}}}. \tag{10}$$

Equation (10) implies that the lifetime of the bubble t_{life} in fully toroidal regimes is largely determined by the popper geometry (h_p/R_p), which makes sense as the popper size is a parameter that determines both the bubble size and the lifetime (Fig. 2). It is also implied that the location of the popper (H/R_p) is another important parameter. This is intuitive as the larger H/R_p allows the popper to release more energy, which is evidenced by the incremental trend of U_{popper} over H/R_p (Fig. 6). Figure 7(b) shows a clear linear relationship with the prediction derived from the scaling analysis. The dashed line is the best-fit line $t_{\text{life}}/[R_p\sqrt{\rho/(p_0 - p_v)}] = 0.179[E/(p_0 - p_v)]^{\frac{1}{2}}(h_p/h)^{\frac{1}{2}}(h_p/R_p)^{\frac{3}{4}}(1 - H/R_p)^{\frac{3}{4}} + 0.335$. Despite the uncertainties mentioned above, the model captures the incremental trend of the bubble lifetime. This suggests that the bubble lifetime is scaled as a function of the popper dynamics. In other words, the parameter H/R_p, which is a measure of the intensity of the interaction between the popper and the substrate, can dominate the bubble morphology as long as other parameters including E and h_p remain constant. The improved linearity is reflected in a better R-square value of 0.69 in Fig. 7(b), up from the raw data's value of 0.41 in Fig. 2(b).

Again, we would emphasize that the above scaling is applicable only to fully toroidal cavitation with intermediate H/R_p values. At small $H/R_p \leqslant 0.4$, the popper makes contact with the substrate while its speed remains relatively slow, leading to either no cavitation or partial cavitation formation. It is also observed that, for poppers without a hole at their apex, similar phenomena occur at slightly larger H/R_p values (see Appendix G). This occurs because, for sufficiently small H, the elastic energy remains stored within the popper and is not transferred to the surrounding water. Consequently, our approach may not be entirely appropriate since it assumes that the energy is fully released into the water. The threshold might also be related to the flexibility of the platform (see Appendix A), which we have not explored in detail. Conversely, at large H/R_p, the popper expels a water jet accompanied by a vortex ring. In such scenarios, all the stored elastic energy is released into the outer fluid region. However, unlike in the case of toroidal cavitation, this energy does not concentrate in the narrow space between the popper and the substrate beneath, leading to different fluid dynamics.

IV. CONCLUSION AND DISCUSSION

We demonstrated that the underwater slamming of a rubber popper toy against a glass substrate can induce a toroidal cavitation bubble (Figs. 1 and 4). A series of experiments (Fig. 3) indicated that the toroidal cavitation occurs due to a fast liquid flow squeezed out from a thin gap between the rubber popper and the glass substrate (Figs. 4–6). As the initial position of the rubber popper in the experiment (H/R_p) increased, the bubble dynamics transfered from the toroidal one to the vortex-ring-type one [Figs. 4(b) and 4(c)]. We found the bubble lifetime (t_{life}) and radii (R_{in} and R_{out}) for the toroidal cavitation and the transient one to be interrelated through the axisymmetric Rayleigh-Plesset-type model [Fig. 7(a)]. We also discussed an analytical framework for this uniquely formed cavitation through the energy balance between the deformed rubber popper and the fully expanded cavitation bubble. The parameter H/R_p, which scales the elastic potential energy used to form cavitation, captured the qualitative trend of both the popper and the bubble dynamics [Fig. 7(b)]. This paper might provide a platform for further studies on bubbles formed in a complex system with the involvement of elastic structures that may include the Mantis Shrimp fist [44] or the brain system [45].

For future work, a systematic investigation into the impact of each parameter is needed. Given the multitude of factors influencing the scaling [as outlined in Eq. (10)], this area warrants further exploration with a broader range and more precise control of the parameters involved. In addition to the influence of popper properties (i.e., Young's modulus E and the thickness h_p), one might be interested in the effect of the indentation depth e as partly discussed above. In [42], there could be two different scaling laws based on the size of e. When $e > h_p$, the shell might form a circular fold around the center, where energy would be concentrated at the rim. On the other hand, a smaller $e < h_p$ can lead to localized deformation at the shell's top, with energy evenly distributed in the deformed region. In our experiments, we can estimate the threshold height, H_{th}, $H_{\text{th}}/R_p \sim (R_p - h_p)/R_p \sim 0.81$, for a smaller popper and $H_{\text{th}}/R_p \sim 0.86$ for a larger popper. Interestingly, this estimated threshold aligns well with our bubble observations (e.g., see Fig. 4) triggering the onset of "cracks" on the bubble surface, suggesting a transition out of the fully toroidal cavitation regime, implying that the rim of the shell would control the bubble. This idea is also supported by the observation that the bubble location and size are intuitive when considering the shape of the deformed shell (see Appendix C). While the data shown in Fig. 7 primarily fall within the fully toroidal regime, a different scaling might be plausible under limited conditions when $H/R_p \sim 1$. In such instances, one could possibly scale $Y_{\text{elastic}} \sim (R_p - H)^2$ [42] instead of using Eq. (9). Although we do not have enough data to validate this, understanding the impact of the indentation depth could provide deeper insight into bubble dynamics. In addition, the energy balance [Eq. (9)] only considers the instantaneous change in energy put into a thin fluid layer. This energy is scaled by the elastic energy stored in the popper right before cavitation when compared to its equilibrium state. As discussed above, the simplification we made poses limitations, which might be related to the ignorance of not only the surrounding fluid flow before cavitation onset but also the subsequent dynamics of the popper. We would also like to acknowledge that, while our energy balance method provides a simplified estimation of the cavitation process, a more comprehensive investigation utilizing the momentum equation with a dynamically deforming boundary is essential for future work.

Most figure files and MATLAB figure data are available on the Open Science Framework [46].

ACKNOWLEDGMENTS

This work was supported by NSF Grants No. CBET-2002714 and No. CMMI-2042740, and JSPS KAKENHI Grant No. JP 23K19089. A.K. is currently at Saitama University where the revised version was finalized. The authors would like to thank H. Ezumi and T. Goto for their assistance in performing the additional experiment. The authors would also like to thank the anonymous reviewers for their insightful and constructive comments.

S.J. conceptualized the work; A.K. designed the experiments; A.K., J.Y., S.W. conducted the experiments and analyzed data, A.K. wrote the original draft of the manuscript, and S.W., J.Y., and S.J. edited the manuscript.

APPENDIX A: PRELIMINARY EXPERIMENT

The preliminary experiment was performed by employing three high-speed cameras synchronized at the frame rate of 5000 frames per second [Fig. 8(a)]. The depth of deionized water was set at approximately 10 cm. A 3D-printed platform [see Fig. 8(b)] was submerged and held by hand. The cross-sectional views of the poppers are shown in Figs. 8(c) and 8(d). As explained, a popper

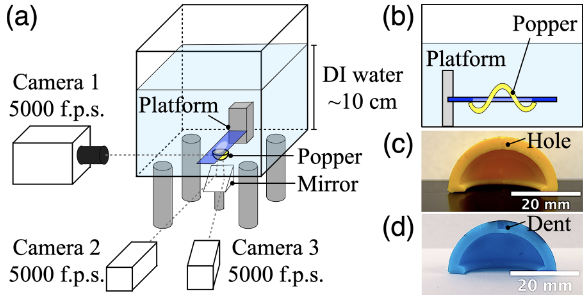

FIG. 8. (a) The experimental setup involves elevating a glass tank and filling it with approximately 10 cm of deionized water. A cantilever structure, including a 3D-printed platform, is submerged to precisely position the rubber popper within the water. Three synchronized high-speed cameras are placed to record both side-view and bottom-view videos of the experiment. All cameras are set to a frame rate of 5000 frames per second. (b) This part of the setup shows a 3D-printed platform, designed to secure the popper at a specific height. The diagram shows a cross-section of the inverted popper. The initial height of the platform sets the parameter H for the experiment. (c),(d) Actual images of the cut popper with (c) and without (d) a hole at the apex. A hole in (c) penetrates the popper top surface, while a dent in (d) is filled at the inner surface of the popper.

has a slight variation in thickness along its arc. The popper used in the main experiment [Fig. 8(c)] has a hole at its apex, which penetrates through the rubbery shell along the axis of symmetry, as marked in the figure. We also show a cross-section of a popper without a hole, used in Appendix G, for comparison [Fig. 8(d)]. As shown, the overall shape including the radius is similar to the one with a hole. The key distinction lies in the design of the top surface: the hole is filled from the inside, creating a dent on the surface. The stiffness of the popper without a hole is briefly discussed in Appendix F, while its bubble formation is detailed in Appendix G.

The snapping process of the popper is illustrated in Fig. 9. For simplicity, we have illustrated only the cross-section of the popper along its centerline. The popper initially stays as a hemispherical shell. We fully invert it and place it on a 3D-printed platform. The platform, having an inner hole slightly smaller in diameter than the popper, can retain the popper against buoyancy. We then allow the popper to snap naturally (as shown by the orange and red curves which depict the approximate popper shape). The snapping time was not actively controlled, but seems to largely depend on the degree of the initial inversion. Due to the platform's constraint, the popper slightly moves down and

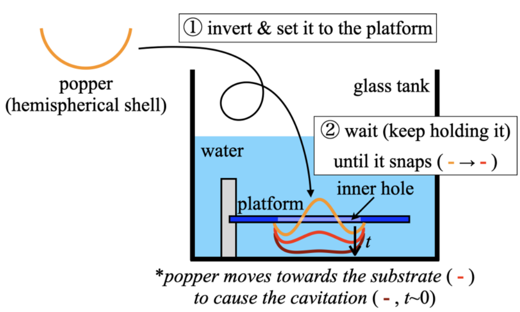

FIG. 9. A schematic illustrating the popper snapping process. For simplicity, the cross-section of the popper along its centerline is depicted. Step ① shows an initially hemispherical popper being inverted and positioned on a platform. In step ②, the popper is allowed to remain until it spontaneously snaps, illustrated by the transition from the orange to the red state. Please note, the time taken for the popper to snap was not controlled. The platform facilitates triggering a toroidal cavitation when it comes sufficiently close to the bottom surface of the glass tank. The approximate state of the popper at $t = 0$ is represented by the brown curve.

creates toroidal cavitation. The brown curve depicts a typical situation right before the formation of cavitation ($t = 0$ ms). We emphasize that the initial distance between the platform and the water tank bottom, denoted as H, serves as the control parameter in this experiment. It significantly influences the extent of popper indentation at the moment of cavitation onset. We acknowledge that the platform's material and clamping method may introduce a degree of flexibility, which could potentially influence the bubble formation outcome. While the role of the platform's flexibility was not a focus of this project, it remains a factor worth considering. It is important to note that we consistently used the same platform throughout the main experiment.

The onset and the collapse of cavitation are visually detected. Thus, the presence of cavitation in this article is defined as the presence of any bubbles, which are larger than a few pixels on the image. The measured data may contain ± 1 frame uncertainty that depends on the individual. The size and the lifetime of the bubble are estimated by using the "reslice" function implemented in the freely available software ImageJ. We assumed the angle made by the two bottom cameras is small enough. We thus directly analyzed either one of these images.

APPENDIX B: TIMESCALE FOR THE POPPER SNAP

The snapping dynamics of the popper, once initiated, lasts for a short duration. The conventional timescale for snapping, proposed for the beam, is $t^* \sim L^2/(h_p\sqrt{E/\rho_{\text{popper}}})$ [21], where L is a characteristic lengthscale for the beam and ρ_{popper} is the density of the popper. We presumed this scaling remains applicable to the spherical shell, substituting L by $2R_p$ [22] to estimate $t^* \sim 5.5$ ms for a smaller popper. Here, we used $E \sim 3.91$ MPa, as measured in Fig. 19, and assumed $\rho_{\text{popper}} \sim 1000$ kg/m^3. While not all experimental videos captured the initial stages of snapping process, we found one specific example ($R_p \sim 16$ mm and $H \sim 18$ mm) demonstrating $t^* \geqslant 10.8 - 11.3$ ms experimentally (see Fig. 10 for details), aligning well with the scaling. It is noteworthy that the snapping dynamics accelerates over time. Towards the end of the snapping process (i.e., just before cavitation onset), the popper speed reaches $U_{\text{popper}} \sim O(10)$ m/s. The popper then oscillates and may trigger the creation of a secondary bubble. The relatively low velocity at $t > 0$ implies the crucial role of the interaction between the popper and the substrate in the generation of toroidal cavitation.

APPENDIX C: ESTIMATION OF THE INVERTED POPPER SHAPE

The basic procedure for the main experiment including the snapping process (Fig. 9) is the same as that for the preliminary experiment. We note that we removed the mirror from the previous setup to help the three-dimensional imaging. The three-dimensional imaging data were correlated through multiple checkerboard images. The vertical (z) axis was determined based on the path of the popper center, which was estimated from one of the experimental data for $H/R_p = 1.13$. Note that $r = 0$ means the popper center. We calculated the radius from the popper center as $r = \sqrt{x_i^2 + y_i^2} - \sqrt{x_0^2 + y_0^2}$ at each time step i (subscript 0 represents the popper center).

We applied the fourth-order polynomial fit to the multiple tracked point to estimate the curved shape of the popper surface (see Fig. 5), which allows us to estimate the location of the extreme R_{rim} as well. We note that, in this manuscript, we only analyzed the surface dots along a single direction to reduce the potential influence of the uneven shape of the popper during snapping. Figure 11 demonstrates how this unevenness, particularly evident at the onset of the snap, can vary [as seen in the comparison of data from four different directions on the same popper in Fig. 11(b)]. Over time, the popper tends to adopt a more axis-symmetric shape, especially at the moment of cavitation occurrence ($t = 0$ ms). Though combining all of these data could potentially enhance accuracy precisely at the cavitation moment, we opted to analyze a limited number of dots to capture the broader dynamics of the event.

The three-dimensional imaging data were also used to estimate the bubble radii R_{in} and R_{out}. Due to the restricted angle between two high-speed cameras, we manually measured the typical

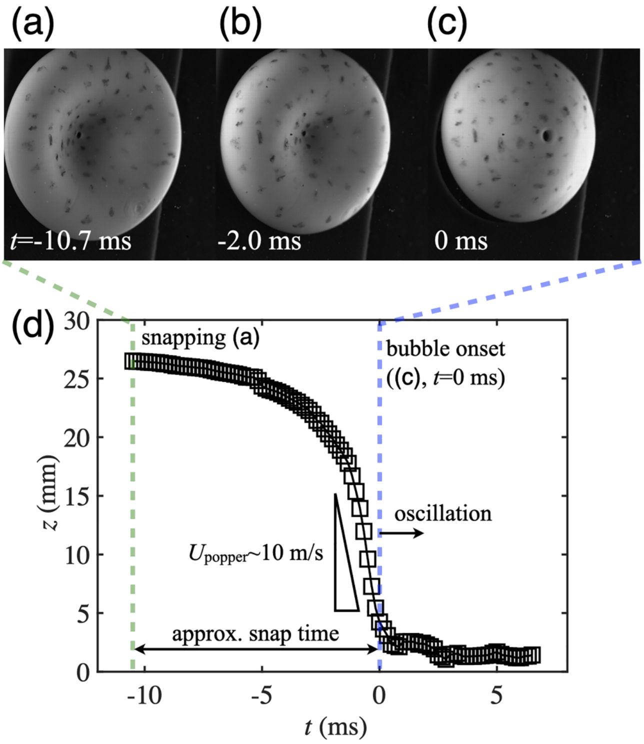

FIG. 10. High-speed images (a)–(c) capture a small popper snapping from a height of approximately $H \sim 18\,\mathrm{mm}$ ($H/R_p \sim 1.13$), highlighting a rapid snap, particularly in the final stage. Please note that $t = 0$ ms is set as one frame before the bubble onset. As $H/R_p \sim 1.13$, the bubble is classified as the vortex-ring-type bubble [refer to Fig. 4(c) for more details]. (d) The tracked location of the popper center in the z-direction. The green line indicates the start of the video, at a point where the snapping has already begun [corresponding to image (a)]. The blue line denotes the timing of the bubble onset [corresponding to image (c)]. The timescale for the popper snapping is estimated as the interval between these two points, roughly around $t^* \geqslant 10.8$ ms. A triangle illustrates a swift snap, especially in the last snapping stage [$\sim O(10)$ ms]. Despite the formation of the vortex-ring-type bubble, the popper continues to oscillate. The magnitude of the z-direction value remains fairly consistent, but the popper may form a secondary toroidal bubble as it approaches the bottom of the glass container again.

bubble radii for each trial through a DLTdv8 digitizing tool [33]. The inner radius R_{in} (squares) is compared with the lowest r-direction value of the estimated popper shape R_{rim} (circles) [Fig. 12(a)]. The black squares and circles are estimated from the same data set, while red and blue squares are shown for comparison purposes. When the bubble maintains the toroidal shape ($H/R_p \leqslant 0.81$), the inner radius R_{in} is close to, or slightly larger than, R_{rim}, suggesting that a fast radial flow developed within a thin gap nucleated cavitation and expelled it outside. In a transition region, a somewhat radial bubble was formed while R_{rim} was not well identified ($H/R_p \geqslant 0.88$). We also show the bubble lifetime t_{life} as a function of H/R_p for both preliminary and main experiments [Fig. 12(b)]. It shows the bubble dynamics in general were well reproduced for various trials. We note that the trend line here was for comparison purposes and was not based on the theoretical background discussed in the paper. We also show the comparison between the rim radius R_{rim} and the inner radius of the cavitation bubble R_{in} in Fig. 13, where a strong correlation is anticipated. This is another representation of the data shown in Fig. 12(a). When the platform height was relatively low ($0.56 \leqslant H/R_p \leqslant 0.81$, referred to as the "fully toroidal" regime in Fig. 13), a consistent trend was observed, indicated by a blue line. This observation is in line with our hypothesis that toroidal

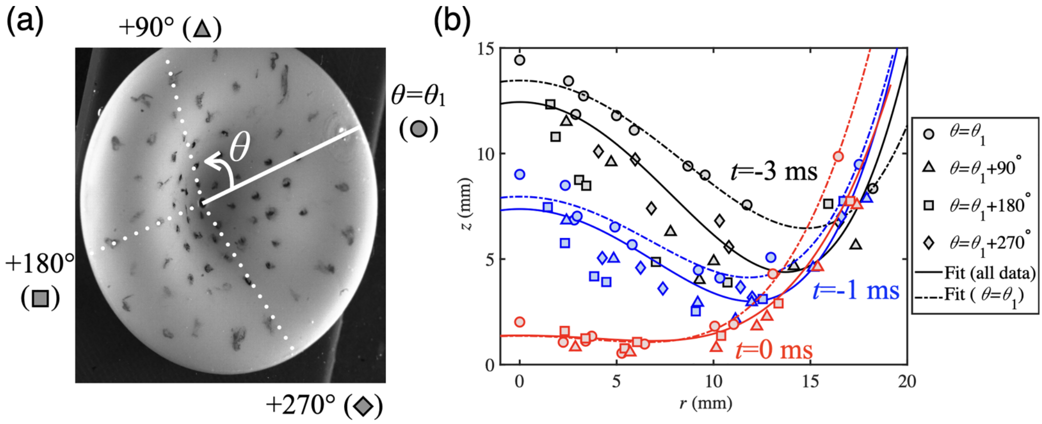

FIG. 11. (a) Shape reconstruction was performed along four different angles; each line is separated by approximately 90° for $H = 12$ mm. The image taken at $t = -15.5$ ms is shown as an example. Data at $\theta = \theta_1$ (equivalent to the condition in Fig. 5) are denoted by circles. The other three lines are marked by triangles ($\theta \approx \theta_1 + 90^\circ$), squares ($\theta \approx \theta_1 + 180^\circ$), and diamonds ($\theta \approx \theta_1 + 270^\circ$). (b) The reconstructed shape is based on 30 data points combining all four lines shown in (a). Different marker shapes indicate four different angles as indicated in (a). The colors indicate different times relative to the onset of cavitation. Solid and dashed lines show the fourth-order polynomial fits for the combined data and the data for $\theta = \theta_1$, respectively.

cavitation initially occurs as attached (or sheetlike) cavitation from the popper surface's lowest point, which scales with R_{rim} at the onset of cavitation. On the other hand, as the H/R_p ratio increased and transitioned into the intermediate regime ($H/R_p \geqslant 0.88$, termed the "transition to vortex ring-type" regime in Fig. 13), we noted a significant reduction in R_{rim} relative to the bubble size. This observation is consistent with our earlier discussions, highlighting that the fast flow between the popper and substrate becomes less significant in the transition regime, suggesting a different onset mechanism, as seen in Fig. 6.

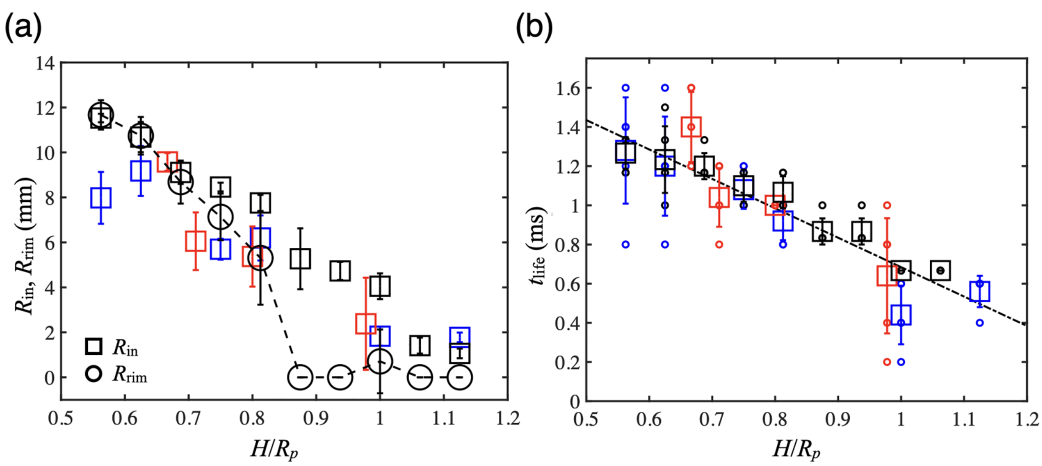

FIG. 12. (a) A comparison between the inner radius R_{in} [squares, see Fig. 2(a)] and the location of the extreme of the polynomials for the popper bottom shape R_{rim} [circles, see Fig. 5(b)] as a function of the platform height H/R_p. Both radii match well as long as cavitation maintains the toroidal shape ($H/R_p \leqslant 0.81$). (b) The lifetime of the bubble as a function of H/R_p with a trend line of $t_{\mathrm{life}} = -1.502\,(H/R_p) + 2.186$ (R-squared value: 0.683).

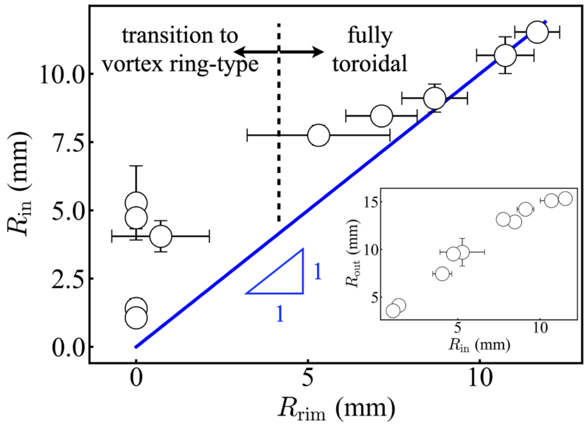

FIG. 13. A comparison between the bubble's inner radius R_{in} and the inverted popper rim's radius R_{rim} immediately prior to the onset of cavitation. Circles represent the data taken from the three-dimensional imaging performed at 6000 frames per second. A blue line shows $R_{\mathrm{in}} = R_{\mathrm{out}}$ for comparison. The dotted line and arrowheads help delineate the threshold between fully toroidal cavitation ($H/R_p \leqslant 0.81$) and the transition to vortex ring-type cavitation ($H/R_p \geqslant 0.88$), as discussed in the main text. The inset shows a comparison of R_{in} and the outer radius of the bubble R_{out}.

It is worth noting that we still observed an incremental relationship between R_{in} and R_{out} (shown in the onset), even when the bubble mechanism differs from the fully toroidal regime. This finding implies that the bubble dynamics predominantly exhibits radial behavior and supports the rationale behind the robust scaling of Eq. (5).

Another notable aspect is the critical role of the popper shell's deformation in bubble formation. As mentioned in the Conclusion section and elaborated in [42], the magnitude of the indentation depth e is pivotal in determining which of two scaling laws is preferred to be adopted. In our experiments, the estimated threshold height, H_{th}, scales as $H_{\mathrm{th}}/R_p \sim (R_p - h_p)/R_p \sim 0.81 - 0.86$, which fairly agrees with the transition observed in the experiment. Also, the observation of the size of the bubble might support this idea. In cases of fully toroidal cavitation ($e > h_p$), as mentioned in [42], the width of the ridge of the shell, δ_{rim}, is estimated as $\delta_{\mathrm{rim}} \sim \sqrt{h_p R_p}$, leading to $\delta_{\mathrm{rim}} \sim 6.9$ mm for a smaller popper. This is within the same order of magnitude as the intercept in the inset of Fig. 13 ($\delta_{\mathrm{bubble}} \sim R_{\mathrm{out}} - R_{\mathrm{in}} \approx 5$ mm). This suggests a correlation between the region achieving the highest flow speed and the location where elastic energy is concentrated. In the transition regime ($e < h_p$), this scaling is expected to predict a deformed region radius $r_{\mathrm{rim}} \sim \sqrt{h_p R_p} \sim 6.9$ mm. This prediction is consistent with the minimum values of R_{rim} and R_{in} observed at the transition point in Fig. 13 (near the vertical dotted line, between 5 and 7.5 mm). These correlations support our hypothesis that the deformation of the popper is instrumental in governing the onset of bubble formation.

APPENDIX D: PARTICLE TRACKING

We adopted the particle tracking approach to estimate the speed of the flow within a narrow gap between the popper and the substrate, which was expected to achieve $V_{\mathrm{particle}} \sim O(10)$ m/s to satisfy Ca < 1. The Stokes number St is the ratio between the characteristic timescale of the particle based on the Stokes law t_{particle} and the flow around the obstacle (i.e., the popper) t_{flow}. Thus, we may write

$$St = \frac{t_{\mathrm{particle}}}{t_{\mathrm{flow}}} \sim \left[\frac{\rho_{\mathrm{particle}} d_{\mathrm{particle}}^2}{18\mu}\right] \Bigg/ \left[\frac{D_p}{V}\right]. \tag{D1}$$

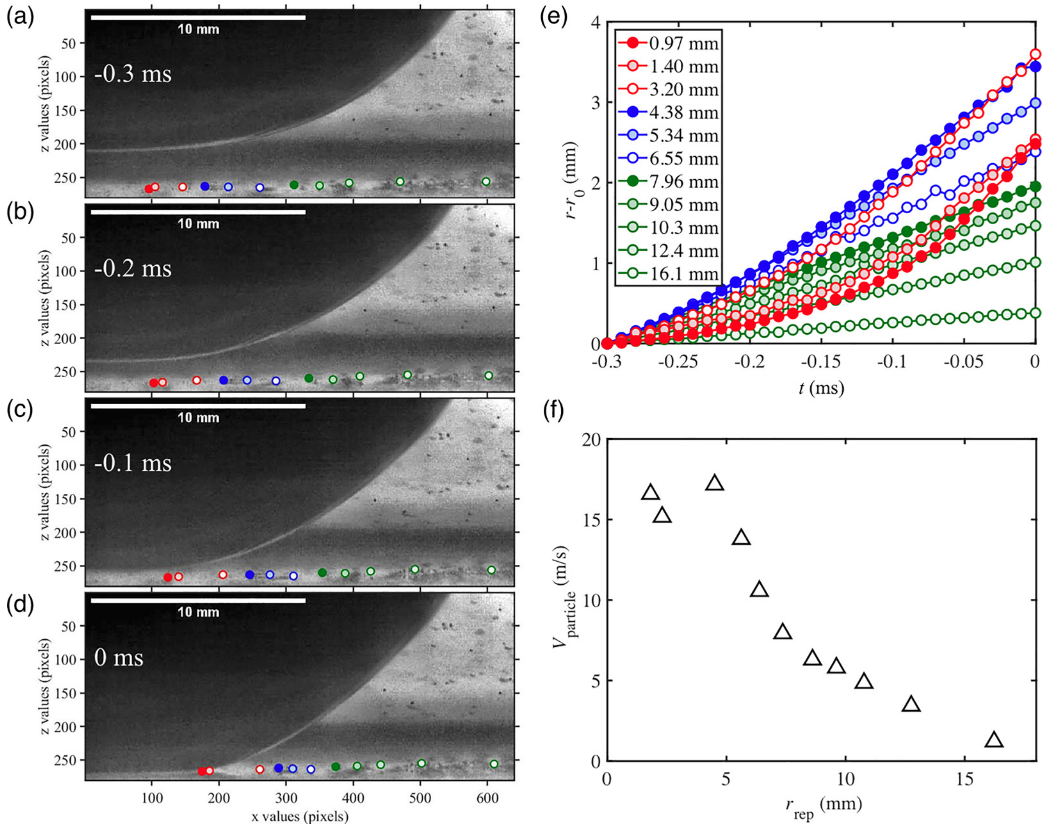

FIG. 14. (a)–(d) Zoom-in images of a popper ($R_p \sim 16$ mm) released from a height of $H \sim 13$ mm. Relative time with respect to the cavitation onset was −0.3 ms (a), −0.2 ms (b), −0.1 ms (c), and 0 ms (d). The silver-coated ceramic particles (d ∼85 μm) mixed in the deionized water enabled particle tracking. The analyzed particles are marked by dots, where the colors are consistent throughout the images. We note that both axes are in pixels to imply the resolution of the image (∼32 pixels/mm). (e) The displacement of the particles from their original position at $t = -0.3$ ms. Numbers in the legend represent the characteristic particle position r_{rep} over the entire course of motions, which is measured at $t = -0.05$ ms. Colors convey the same meanings as those in (a)–(d). (f) The averaged particle velocities over 0.1 ms before the cavitation onset (V_{particle}) as a function of the particle position r_{rep} over the entire course of motions.

Here, the particle density and diameter are assumed to be $\rho_{\mathrm{particle}} \approx 1\times10^3$ kg/m^3 and $d_{\mathrm{particle}} \sim$ 85 μm. The fluid viscosity is $\mu \sim 1\times10^{-3}$ Pa s. D_p is the diameter of the popper, $D_p = 2R_p =$ 32 mm for a smaller popper. The velocity scale V needs to be determined in the experiment, but we approximate this as $V \sim V_r = 10$ m/s considering the order of magnitude for the cavitation onset for simplicity. By plugging these values into the equation above, we obtain $\mathrm{St} \sim 0.13 < 1$. We acknowledge the inherent uncertainty regarding the net particle properties (diameter d_{particle} and density ρ_{particle}) and velocity scale V. However, the order of magnitude would largely remain the same, indicating that this simple estimate should adequately capture the overall traceability. In the analysis, we arbitrarily selected the traceable particles out of five trials for five different H values. Figure 14 shows the typical images of the particle tracking, where the particles tracked are marked by dots (the height H was set to $H = 13$ mm). In this example, we tracked particles at 11 different locations as marked. We note that we selected the particles floating on the glass substrate to estimate the radial flow speed. We acknowledge that the particle motion might be affected by the

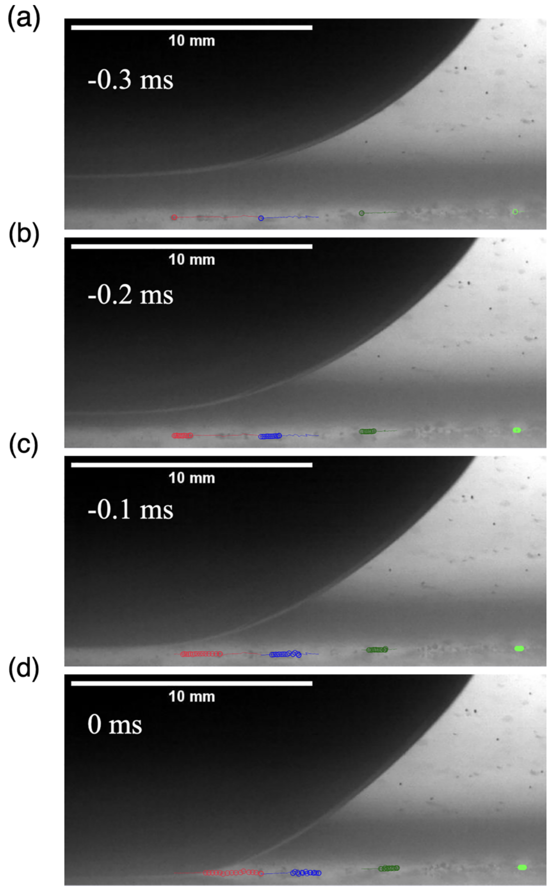

FIG. 15. Here we provide a different visualization of the particle tracking data, as previously shown in Fig. 14. The paths and trajectories for selected particles [specifically the 3rd, 6th, 9th, and 11th from the left as seen in Figs. 14(a)–14(d)] are shown.

viscous boundary layer over the substrate and be decelerated. This analysis reflects the lower bound of the flow speeds. As time progresses, particles move to the right, suggesting that the flow is indeed squeezed away from the popper center. This flow pattern is always the case for multiple trials with different H values.

Figure 14(e) shows the time series of the particle positions. The vertical axis represents the displacement of the particles with respect to their original location at $t = -0.3$ ms. The numbers in the legend show the characteristic location of each particle r_{rep}, which is measured at $t = -0.05$ ms to reflect both their location and speed. Particles located far away from the popper center (green markers) travel at an almost constant speed. The traveling speed of particles decreases as r_{rep} increases (see the blue and green markers). Interestingly, the particle trajectory for particles closer to the popper center shows a slightly different trend (red markers). Particles do not move much at first ($-0.3 \leqslant t \leqslant -0.1$ ms) and then accelerated rapidly ($t \geqslant -0.1$ ms). We set $\Delta t_2 = 0.1$ ms to calculate V_{particle}. Figure 14(f) shows the averaged particle speeds for 0.1 ms V_{particle} as a function of r_{rep}. The speed of outside particles decreases as the distance increases, while inner particles maintain faster speeds. Figures 14(e) and 14(f) suggest that the flow reaches at least $V_r \sim 18$ m/s, causing cavitation.

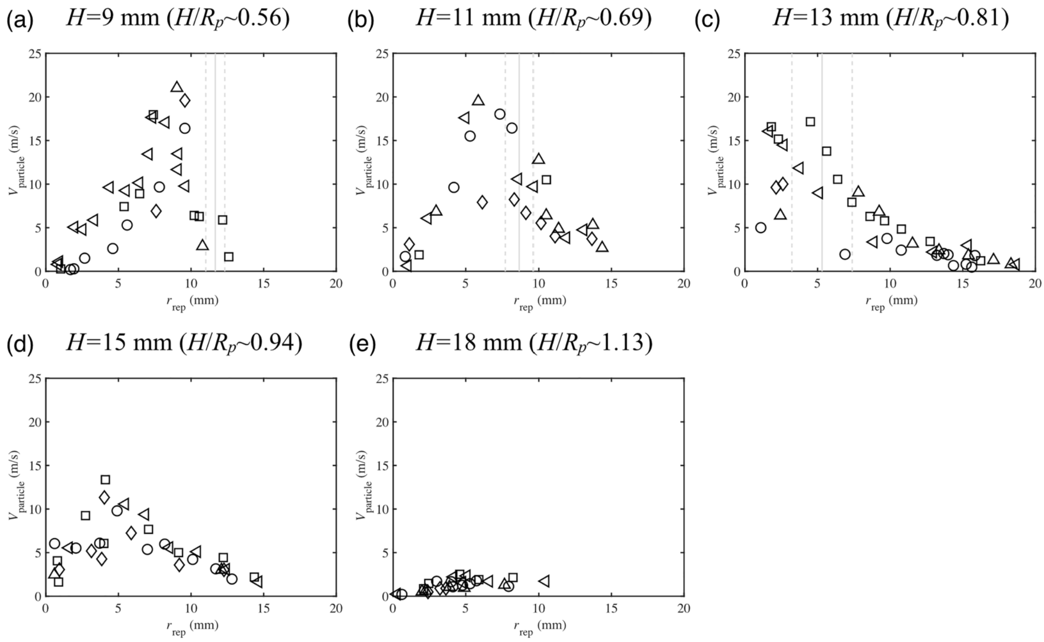

FIG. 16. Particle speeds V_{particle} for various cases vs the characteristic particle location r_{rep}. Each panel (a)–(e) contains the data from five different runs for each release height H. Each marker represents an individually tracked particle, with the shape of the markers differentiating each experimental run. It is important to note that the number of tracked particles varied with each attempt. Solid and gashed gray lines (when available) represent the mean and standard deviation of R_{rim} data. We observed a formation of either toroidal cavitation or the transition cavitation upon the first stretch of the popper for (a)–(d) ($0.56 \leqslant H/R_p \leqslant 0.94$), while a ring bubble was formed when $H/R_p \sim 1.13$.

Figures 15(a)–15(d) show another representation of the particle tracking data, where they are shown in Figs. 14(a)–14(d). The paths and trails are visualized by using the tracker software. For simplicity, we have chosen only four particles from $t = -0.3$ to 0 ms. As previously discussed in Fig. 14(e), a particle near the rim (indicated in red in Figs. 14 and 15) experiences acceleration just prior to the onset of cavitation (comparing $t = -0.1$ and 0 ms panels in Fig. 15). Additionally, Fig. 15 reveals that the velocity of the particles (i.e., the radial velocity of the squeezed flow) diminishes as the distance from the center of the popper increases [also see Figs. 14(e) and 14(f)].

As represented by Fig. 14(e), the particle speed V_{particle} reaches the maximum at a certain distance r from the popper center. It is interesting to note that the peak shifts to a smaller r as H increases [Figs. 16(a)–16(c)]. In Fig. 16, individual markers stand for each tracked particle, with different shapes indicating separate experimental runs. This is intuitive from the trend shown in Fig. 6(b), i.e., the radius of the thinnest gap R_{rim} shrinks as H/R_p increases. Solid and dashed gray lines in Figs. 16(a)–16(c) represent the mean and standard deviation of R_{rim} estimated by the three-dimensional imaging [Fig. 6(b)], showing a qualitative agreement. R_{rim} values for $H/R_p \sim 0.94$ and 1.13 were not available as discussed. They showed the reduction in speed for larger H/R_p and the outward shift of the peak.

APPENDIX E: FORCE UPON THE POPPER SNAP

We measured the force upon the popper snap in air to support establishing the scaling. For this measurement, calibration for the force sensor was performed by using the weight balances to convert units from signal output (S.O.) (V) to force (N), where the result is shown in Fig. 17(a). We varied

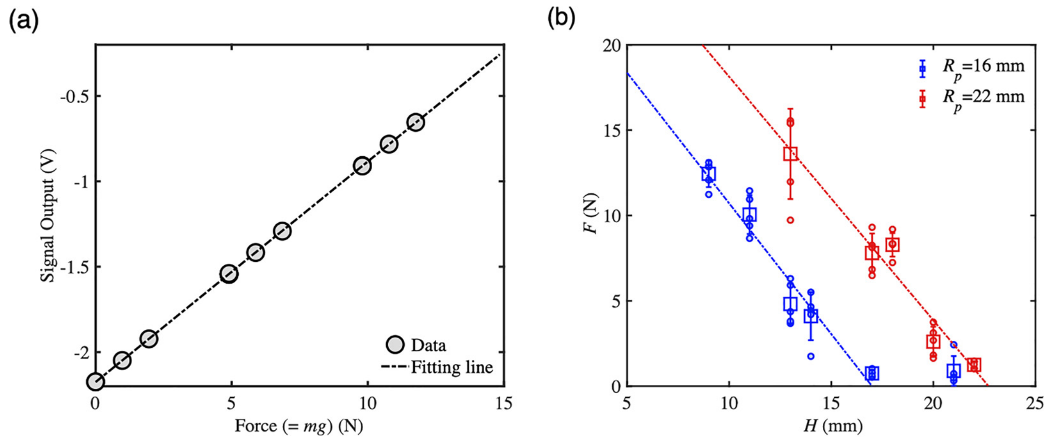

FIG. 17. (a) A calibration curve between the signal output from the force sensor (S.O.) and the force estimated by the weight ($F = mg$). The fitting line is estimated to be S.O. $= 0.1292F - 2.1757$. (b) Measured forces as a function of the platform position H, where the colors distinguish the popper sizes. The trend lines are estimated to be $F = -1.531H + 26.02$ ($R^2 = 0.9188$) for $R_p = 16$ mm (blue) and $F = -1.427H + 32.4$ ($R^2 = 0.8869$) for $R_p = 22$ mm (red). We note that we excluded the data for $H = 21$ mm when obtaining the fitting curve for a smaller popper ($R_p = 16$ mm). We note that we have five trials at each condition (marked by dots) to obtain the average value (square) and standard deviation (error bar).

the mass of the weight balances from 0.2 to 1.2 kg. The calibration curve (a dashed line) is S.O. $=$ $0.1292F - 2.1757$. The dimensional result based on the calibration curve is shown in Fig. 17(b) for both popper sizes. Two dashed lines are demonstrating the downward trends. It was obvious that the impulsive force F becomes smaller as H increases. Also, the larger popper ($R_p = 22$ mm) can cause a larger force when compared to the one with a smaller popper ($R_p = 16$ mm). Figure 17(b) demonstrates that the height H and the popper size R_p govern the impulsive force F as discussed in the main manuscript. Note that we made a crude assumption that the scaling relationship between F and H/R_p does not change in either air or underwater, in order to apply the findings to the current problem.

Figure 18 compares the normalized force, $F' \sim \frac{1}{T}\int F\,dt\, R_p^{\frac{1}{2}}/(Eh_p^{\frac{5}{2}})$, measured in air for various H/R_p for two different popper sizes. The normalized force is scaled based on Eq. (9) as follows:

$$\frac{1}{T}\int F dt \left[\frac{1}{Eh_p^2}\right]\left[\frac{R_p}{h_p}\right]^{\frac{1}{2}} \sim \left(1 - \frac{H}{R_p}\right)^{\frac{1}{2}}. \tag{E1}$$

We note that we employ the impulse ($\frac{1}{T}\int F\,dt$) instead of the instantaneous maximum force F to represent the overall force within a short time, while the duration for the force remains within the same order of magnitude (less than 1 s). Here the impulse is thus a measure of the averaged force over time. The left side of the above equation represents the force generated, normalized by the characteristic force scale determined by the popper's properties. The right side signifies the experimental condition governed by the stand-off distance. Figure 18 presents data for larger and smaller poppers, represented in red and blue, respectively, as also depicted in Fig. 17. A black dashed line represents the fitted line [$F' \sim 0.637(1 - H/R_p)^{1/2} - 0.031$], estimated using the curve-fitting toolbox in MATLAB. We should note that we excluded data for $H/R_p > 1$, where the force F tends to be very small and $1 - H/R_p$ assumes a negative value. As depicted, the force increases with increasing $1 - H/R_p$, reaching a near-zero value at $1 - H/R_p \sim 0$, which aligns with the geometrical constraints. Even though our data are somewhat limited, the general upward trend

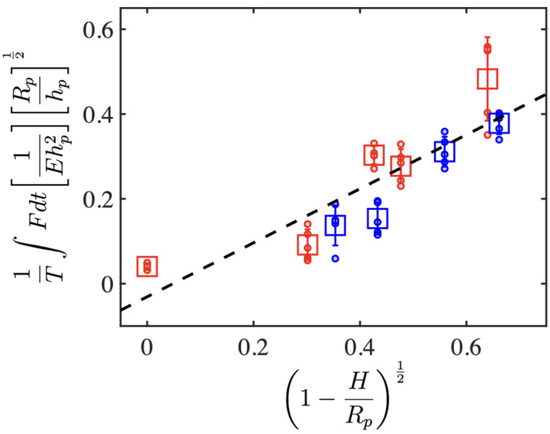

FIG. 18. A comparison between the normalized force $F' = \frac{1}{T}\int F\, dt\, R_p^{\frac{1}{2}}/(Eh_p^{\frac{5}{2}})$ (measured in air) vs the stand-off parameter $(1 - H/R_p)^{1/2}$. The squares are the mean value derived from five trials, indicated by the dots. The error bars represent the standard deviation. Different colors differentiate between the typical sizes of the popper at rest, consistent with those in Fig. 17. The dashed line shows a fitting $F' \sim 0.637(1 - H/R_p)^{\frac{1}{2}} - 0.031$ (R-squared value: 0.716).

observed in Fig. 18 suggests that H/R_p can indeed regulate the intensity of the interaction between the popper and the substrate, as discussed earlier.

APPENDIX F: ELASTIC MODULUS OF THE RUBBER POPPER

We estimate the elastic modulus of the rubber poppers used in our experiments. To facilitate this, we prepared poppers cut along their arch. One end of each cut popper was glued tightly onto a platform, while the other end was pushed vertically using a narrow needle [see Fig. 19(a)]. The dimensions of the popper (b_{beam}, h_{beam}) are separately measured. We may consider this as a curved-beam problem [47,48], where we can find the relationship between the force F and the vertical

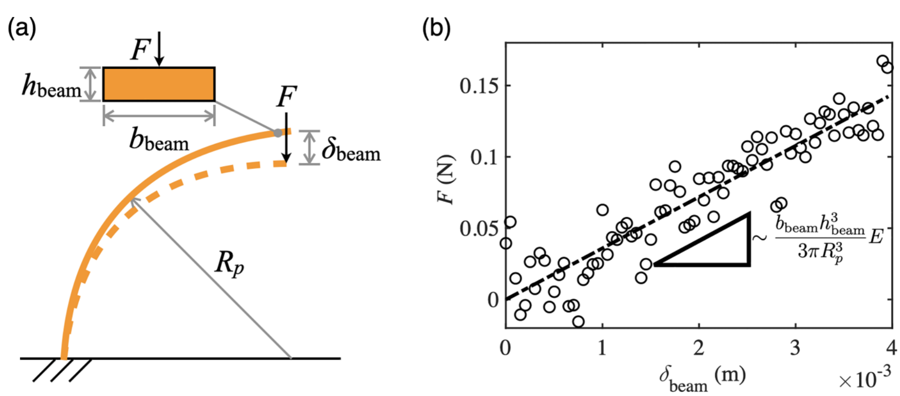

FIG. 19. (a) A schematic of the curbed beam system with the popper radius R_p, local width b_{beam}, and h_{beam} of the cut popper near the tip, where the force F is being applied continuously to record deflection δ_{beam}. (b) A typical result with a cut popper, where Young's modulus might be scaled by taking the slope of the $F - \delta_{\text{beam}}$ curve.

deflection δ_{beam} as

$$\delta_{\mathrm{beam}} = \frac{F\pi R_p^3}{4EI}, \tag{F1}$$

where the second moment of area is $I = b_{\mathrm{beam}} h_{\mathrm{beam}}^3/12$. Thus, we may reformulate the relationship above as

$$F = \left[\frac{4EI}{\pi R_p^3}\right]\delta_{\mathrm{beam}} = \left[\frac{b_{\mathrm{beam}} h_{\mathrm{beam}}^3}{3\pi R_p^3} E\right]\delta_{\mathrm{beam}}. \tag{F2}$$

Therefore, by obtaining the slope of the force (F) versus indentation (δ_{beam}) curve, we can estimate Young's modulus of the popper.

To measure the force and deflection, we used an Instron machine (model 5965, Instron Corporation, Norwood, MA) with a needle-type attachment. The radius of the curved beam was assumed to be $R_p \approx 16$ mm. In terms of the second moment of area, we used the local dimensions of the beam (b_{beam}, h_{beam}) at the location of the force application. Figure 19(b) shows a typical result from measuring a cut popper, which comes from the same supplier as the one we used in the main experiment. The vertical axis represents the force F, while the horizontal axis shows the deflection δ_{beam}. It is important to note that the origin of the axes is offset to ensure that the fitting curve demonstrates a linear relationship without an intercept, solely for clarity in presentation. Additionally, we restricted our analysis to data where $\delta_{\mathrm{beam}} \leqslant R_p/4 \approx 4$ mm. Upon testing two different poppers from this supplier, each measured three times, we determined that Young's modulus for the smaller poppers in our main experiment can be estimated to range between $E = 3.57$ and 4.28 MPa. For the purposes of this paper, we adopted $E \sim 3.91$ MPa as a more representative or estimated value of the popper's stiffness, based on these findings.

In addition, we conducted measurements on one popper without a hole (see Appendix G) and found $E = 2.95 - 3.22$ MPa. This value is marginally lower than that of the popper with a hole, yet the difference may not be significant. This is because the scaling suggests that the influence of E on the bubble lifetime is proportional to the square root of E, or $E^{1/2}$.

APPENDIX G: INFLUENCE OF THE HOLE AT THE APEX OF THE POPPER

As mentioned in the text, the hole at the apex plays an important role in the formation of the vortex ring-type bubble. We experimentally assessed the influence of the hole at the apex of the popper. A popper without a hole has almost comparable dimensions to the smaller popper with a hole [$R_p \sim 16$ mm, $h_p \sim 3$ mm, where the cross-sectional image is shown in Fig. 8(d)]. The stiffness of the poppers varied, as reported in Appendix F. We built a 3D printed platform similar to that in the main experiment. We used a glass fish tank and partially filled it with tap water. We employed a Photron SA5 high-speed camera (10 000 f.p.s., 0.05–0.07 mm/pixel) through a mirror placed underneath the fish tank with an inclination of 45° (i.e., bottom-view), which provides the lifetime and radii of the toroidal bubbles.

We compared the bubble lifetime T_{life} and the inner radius R_{in} as a function of H for poppers both with and without a hole. Black and green markers, respectively, show the average values from at least five trials for each point. In Fig. 20(a), this comparison reveals that both types of poppers generally produce similar bubbles, except in cases with smaller H values. Here, instead of forming fully toroidal bubbles, they result in partial ones. We realized that the popper dynamic is significantly affected by its asymmetric shape during snapping, leading to varied partial bubble formations. While we cannot draw definitive conclusions due to limited data, these dynamics appear to be dependent on the popper's design or material. Most of the data show similar trends up to $H \leqslant 16$ mm, with the hole-free popper (green squares) demonstrating a decremental trend that aligns with the fitted curve of the holed popper (black squares). However, detailed analysis reveals potential effects of the hole. As indicated in Fig. 20(b), the inner bubble radius R_{in} for the holed popper tends to be larger

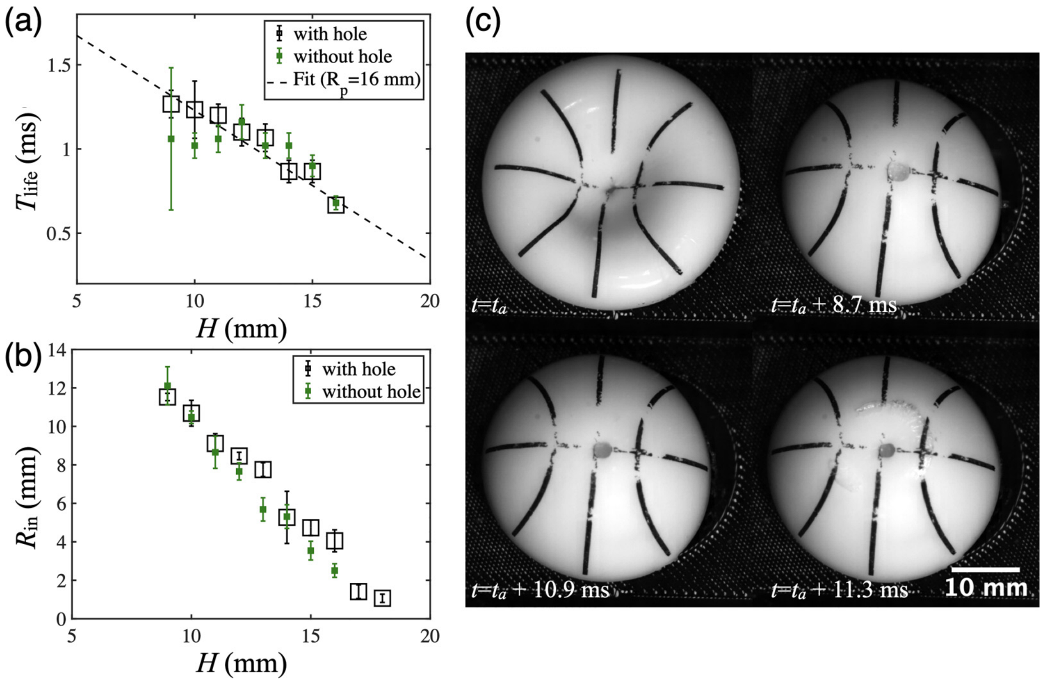

FIG. 20. (a) Comparison of bubble lifetime T_{life} as a function of the initial platform height H for the poppers with and without a hole at the apex. A dashed line represents the empirical fit for the popper with a hole, as witnessed in Fig. 2(b). (b) Comparison of the inner bubble radius R_{in} as a function of H for two different poppers. (c) Typical images of a popper without a hole activated at $H = 18$ mm ($t = t_a$), where only the secondary cavitation ($t = t_a + 11.3$ ms) was observed. Note that a dent at the popper center is sealed on the back side by design, meaning that the leakage of the fluid through the popper center is assumed to be negligible.

than that of the hole-free popper at $H \sim 15 - 16$ mm, despite similar lifetimes. We speculate that this difference might arise because the sealed hole restricts the top part of the popper from opening fully, thus limiting its lateral expansion.

Another observation relates to the popper without a hole, which does not generate a vortex ring-type bubble at $H > 1$ [as shown in Fig. 20(c)]. Figure 20(c) illustrates the typical dynamics of a popper without a hole activated at $H \sim 18$ mm. Although there appears to be a hole at its apex, it is closed on the inner side [refer to Fig. 8(d)], preventing fluid escape. Since cavitation onset was not confirmed, we use $t = t_a$ as a reference point instead of $t = 0$. The top images suggest the popper completes its first movement within approximately 8.7 ms [see Fig. 20(c)]. The popper then starts to oscillate ($t = t_a + 10.9$ ms), preparing for the secondary snap. It is important to note that there is no vortex ring-type cavitation bubble up to this stage. We could see an air pocket in a hole, however it is not very visible and does not expel into the surrounding fluid. This absence of a vortex-ring-type bubble aligns with our discussion in Sec. III A [Fig. 1(c)] that such bubbles are typically caused by rapid liquid flow through the popper's hole. In the absence of a hole, the top part of the popper remains intact, allowing only for the pushing of fluid and thus precluding the formation of a ring-type bubble. At $t = t_a + 11.3$ ms, the popper interacts with the substrate, creating secondary cavitation with a somewhat annular shape, similar to that seen with the popper with a hole. This indicates that the fundamental bubble dynamics are qualitatively similar for poppers with and without a hole, except in conditions where $H/R_p \gtrsim 1$.

[1] C. Brennen, *Cavitation and Bubble Dynamics* (Oxford University Press, Oxford, 1995).

[2] L. A. Teran, S. A. Rodríguez, S. Laín, and S. Jung, Interaction of particles with a cavitation bubble near a solid wall, Phys. Fluids **30**, 123304 (2018).

[3] L. A. Teran, S. Laín, S. Jung, and S. A. Rodríguez, Surface damage caused by the interaction of particles and a spark-generated bubble near a solid wall, Wear **438-439**, 203076 (2019).

[4] A. D. Maxwell, T.-Y. Wang, C. A. Cain, J. B. Fowlkes, O. A. Sapozhnikov, M. R. Bailey, and Z. Xu, Cavitation clouds created by shock scattering from bubbles during histotripsy, J. Acoust. Soc. Am. **130**, 1888 (2011).

[5] C. D. Ohl, M. Arora, R. Dijkink, V. Janve, and D. Lohse, Surface cleaning from laser-induced cavitation bubbles, Appl. Phys. Lett. **89**, 074102 (2006).

[6] J. J. Lee, J. D. Eifert, S. Jung, and L. K. Strawn, Cavitation bubbles remove and inactivate listeria and salmonella on the surface of fresh roma tomatoes and cantaloupes, Front. Sustain. Food Syst. **2**, 61 (2018).

[7] R. Blake and D. C. Gibson, Cavitation bubbles near boundaries, Annu. Rev. Fluid Mech. **19**, 99 (1987).

[8] O. Supponen, D. Obreschkow, M. Tinguely, P. Kobel, N. Dorsaz, and M. Farhat, Scaling laws for jets of single cavitation bubbles, J. Fluid Mech. **802**, 263 (2016).

[9] O. Supponen, D. Obreschkow, P. Kobel, M. Tinguely, N. Dorsaz, and M. Farhat, Shock waves from nonspherical cavitation bubbles, Phys. Rev. Fluids **2**, 093601 (2017).

[10] O. Supponen, D. Obreschkow, and M. Farhat, Rebounds of deformed cavitation bubbles, Phys. Rev. Fluids **3**, 103604 (2018).

[11] S. Poulain, G. Guenoun, S. Gart, W. Crowe, and S. Jung, Particle motion induced by bubble cavitation, Phys. Rev. Lett. **114**, 214501 (2015).

[12] G. T. Bokman, O. Supponen, and S. A. Mäkiharju, Cavitation bubble dynamics in a shear-thickening fluid, Phys. Rev. Fluids **7**, 023302 (2022).

[13] A. Žnidarčič R. Mettin, C. Cairós, and M. Dular, Attached cavitation at a small diameter ultrasonic horn tip, Phys. Fluids **26**, 023304 (2014).

[14] J. Morton, M. Khavari, A. Priyadarshi, A. Kaur, N. Grobert, J. Mi, K. Porfyrakis, P. Prentice, D. Eskin, and I. Tzanakis, Dual frequency ultrasonic cavitation in various liquids: High-speed imaging and acoustic pressure measurements, Phys. Fluids **35**, 017135 (2023).

[15] M. Versluis, B. Schmitz, A. von der Heydt, and D. Lohse, How snapping shrimp snap: through cavitating bubbles, Science **289**, 2114 (2000).

[16] P. Koukouvinis, C. Bruecker, and M. Gavaises, Unveiling the physical mechanism behind pistol shrimp cavitation, Sci. Rep. **7**, 13994 (2017).

[17] G. N. Kawchuk, J. Fryer, J. L. Jaremko, H. Zeng, L. Rowe, and R. Thompson, Real-time visualization of joint cavitation, PLoS ONE **10**, e0119470 (2015).

[18] T. W. Randolph, Do not drop: Mechanical shock in vials causes cavitation, protein aggregation, and particle formation, J. Pharm. Sci. **104**, 602 (2015).

[19] A. Kiyama, Y. Tagawa, K. Ando, and M. Kameda, Effects of a water hammer and cavitation on jet formation in a test tube, J. Fluid Mech. **787**, 224 (2016).

[20] Z. Pan, A. Kiyama, Y. Tagawa, D. Daily, S. Thomson, R. Hurd, and T. Truscott, Cavitation onset caused by acceleration, Proc. Natl. Acad. Sci. USA **114**, 8470 (2017).

[21] M. Gomez, D. E. Moulton, and D. Vella, Critical slowing down in purely elastic 'snap-through' instabilities, Nat. Phys. **13**, 142 (2017).

[22] A. Pandey, D. E. Moulton, D. Vella, and D. P. Holmes, Dynamics of snapping beams and jumping poppers, Europhys. Lett. **105**, 24001 (2014).

[23] B. Gorissen, D. Melancon, N. Vasios, M. Torbati, and K. Bertoldi, Inflatable soft jumper inspired by shell snapping, Sci. Robot. **5**, eabb1967 (2020).

[24] Y. Kim, J. Berg, and A. J. Crosby, Autonomous snapping and jumping polymer gels, Nat. Mater. **20**, 1695 (2021).

[25] K. L. De Graaf, P. A. Brandner, J. Y. Lee, and B. W. Pearce, Cavitation about a sphere impacting a flat surface, in *Proceedings of 19th Australasian Fluid Mechanics Conference* (Australasian Fluid Mechanics Society, 2014).

[26] K. L. De Graaf, P. A. Brandner, B. W. Pearce, and J. Y. Lee, Cavitation due to an impacting sphere, in *Journal of Physics: Conference Series* (IOP, Bristol, UK, 2015), p. 012014.

[27] M. M. Mansoor, J. O. Marston, J. Uddin, G. Christopher, Z. Zhang, and S. T. Thoroddsen, Cavitation structures formed during the collision of a sphere with an ultra-viscous wetted surface, J. Fluid Mech. **796**, 473 (2016).

[28] M. M. Mansoor, J. Uddin, J. O. Marston, I. U. Vakarelski, and S. T. Thoroddsen, The onset of cavitation during the collision of a sphere with a wetted surface, Exp. Fluids **55**, 1648 (2014).

[29] J. R. T. Seddon, M. P. Kok, E. C. Linnartz, and D. Lohse, Bubble puzzles in liquid squeeze: Cavitation during compression, Europhys. Lett. **97**, 24004 (2012).

[30] A. Kiyama, S. Wang, and S. Jung, "pop" goes the toroidal bubble, in *75th Annual Meeting of the APS Division of Fluid Dynamics* (Gallery of Fluid Motion, Indianapolis, 2022), p. P0037.

[31] ArtCreativity.com

[32] M. L. Sheely, Glycerol viscosity tables, Ind. Eng. Chem. **24**, 1060 (1932).

[33] T. L. Hedrick, Software techniques for two- and three-dimensional kinematic measurements of biological and biomimetic systems, Bioinspir. Biomimet. **3**, 034001 (2008).

[34] D. Brown and A. J. Cox, Innovative uses of video analysis, Phys. Teach. **47**, 145 (2009).

[35] J. O. Marston, I. U. Vakarelski, and S. T. Thoroddsen, Cavity formation by the impact of leidenfrost spheres, J. Fluid Mech. **699**, 465 (2012).

[36] F. M. White and H. Xue, *Fluid Mechanics*, 9th ed. (McGraw-Hill Education Publisher, New York, 2021).

[37] L. Rayleigh,VIII. on the pressure developed in a liquid during the collapse of a spherical cavity, London, Edinburgh Dublin Philos. Mag. J. Sci. **34**, 94 (1917).

[38] M. S. Plesset, The dynamics of cavitation bubbles, J. Appl. Mech. **16**, 277 (1949).

[39] G. L. Chahine and P. F. Genoux, Collapse of a cavitating vortex ring, J. Fluids Eng. **105**, 400 (1983).

[40] D. Lohse, R. Bergmann, R. Mikkelsen, C. Zeilstra, D. van der Meer, M. Versluis, K. van der Weele, M. van der Hoef, and H. Kuipers, Impact on soft sand: Void collapse and jet formation, Phys. Rev. Lett. **93**, 198003 (2004).

[41] V. Duclaux, F. Caille, C. Duez, C. Ybert, L. Bocquet, and C. Clanet, Dynamics of transient cavities, J. Fluid Mech. **591**, 1 (2007).

[42] B. Audoly and Y. Pomeau, *Elasticity and Geometry: From hair curls to the non-linear response of shells* (Oxford University Press, Oxford, 2010).

[43] L. Stein-Montalvo, D. P. Holmes, and G. Coupier, Delayed buckling of spherical shells due to viscoelastic knockdown of the critical load, Proc. R. Soc. London A **477**, 20210253 (2021).

[44] S. N. Patek and R. L. Caldwell, Extreme impact and cavitation forces of a biological hammer: strike forces of the peacock mantis shrimp Odontodactylus scyllarus, J. Exp. Biol. **208**, 3655 (2005).

[45] J. Lang, R. Nathan, D. Zhou, X. Zhang, B. Li, and Q. Wu, Cavitation causes brain injury, Phys. Fluids **33**, 031908 (2021).

[46] DOI 10.17605/OSF.IO/YCNV8

[47] W. C. Young and R. G. Budynas, *Roark's Formulas for Stress and Strain*, 8th ed. (McGraw-Hill, New York, 2002).

[48] I. Nakahara, *Mechanics of Materials (in Japanese)* (YOKENDO, 1965).